Comput. Methods Appl. Mech. Engrg. 200 (2011) 57–76

Contents lists available at ScienceDirect

Comput. Methods Appl. Mech. Engrg.

journal homepage: www.elsevier.com/locate/cma

Mixed perfectly-matched-layers for direct transient analysis in 2D elastic heterogeneous media

S. Kucukcoban, L.F. Kallivokas *

Department of Civil, Architectural and Environmental Engineering, The University of Texas at Austin, 1 University Station, C1748, Austin, TX 78712, USA

ARTICLE INFO

Article history:
Received 23 July 2009
Received in revised form 21 July 2010
Accepted 24 July 2010
Available online 25 August 2010

Keywords:
Unsplit-field perfectly-matched-layers (PMLs)
Mixed finite elements
Transient wave propagation
Semi-infinite domains

ABSTRACT

We are concerned with elastic waves arising in plane-strain problems in an elastic semi-infinite arbitrarily heterogeneous medium. Specifically, we discuss the development of a new mixed displacement–stress formulation for forward elastic wave simulations in perfectly-matched-layer (PML)-truncated heterogeneous media.

To date, most PML formulations split the displacement and stress fields, resulting in non-physical components for each field. In this work, we favor unsplit schemes, primarily for the relative ease by which the resulting forms can be incorporated into existing codes, the ease by which the resulting semi-discrete forms can be integrated in time, and the ease by which they can be used in adjoint formulations arising in inverse problems, contrary to most past and current developments. We start by following classical lines, and apply complex-coordinate-stretching to the governing equations in the frequency domain, while retaining both displacements and stress quantities as unknowns. With the aid of auxiliary variables the resulting mixed form is rendered second-order in time, thereby allowing the use of standard time integration schemes. We report on numerical simulations demonstrating the stability and efficacy of the approach.

1. Introduction

The simulation of wave motion in unbounded heterogeneous media requires negotiation of the infinite or semi-infinite extent of the unbounded domain. When domain discretization methods are used, the reduction of the physical to a finite domain through truncation is the only available computational strategy.[1] Truncation introduces artificial (non-physical) boundaries surrounding the finite computational domain. These boundaries require special treatment in order for the finite domain of interest to mimic the physical behavior of the non-truncated domain, while minimizing spurious reflections that may pollute the solution within the finite computational domain.

Two distinctly different strategies are possible for dealing with truncation boundaries: either to truncate the semi-infinite extent by introducing a transparent condition at the truncation interface, or to truncate by introducing an absorbing condition or absorbing buffer/layer. A transparent condition allows the passage of waves with, ideally, no or minimal reflections from the interface. An absorbing condition will typically force the decay of the wave motion within a buffer zone, while, ideally, annihilating any interface reflections as well.[2]

Both categories, transparent and absorbing/layer conditions, have their own strengths and limitations. Broadly classified, transparent conditions are either local or non-local, where the non-locality refers to the temporal (convolution) and spatial (boundary integral) coupling of the response at the truncation interface. The published literature on the subject is considerable: Tsynkov [1] provides an excellent review of both local and non-local truncation conditions. Non-local conditions typically attempt to simulate exactly the effect of the infinite (or semi-infinite) medium [2–4], while assuming that the domain excluded from the computations is homogeneous. However, the benefit derived by providing an exact condition comes at a computationally expensive, difficult to implement, scheme. In addition, non-local conditions cannot handle arbitrary heterogeneity. To overcome the difficulties arising with non-local conditions, local conditions tend to relax both the spatial and temporal non-locality, but result in approximate forms that allow for reflections [5–9]. Local conditions are less accurate, but computationally efficient, and easy to implement when they

* Corresponding author.
E-mail addresses: ksezgin@mail.utexas.edu (S. Kucukcoban), loukas@mail.utexas.edu (L.F. Kallivokas).

[1] Domain discretization methods are, essentially, the only possibility when the domain is heterogeneous.

[2] Transparent conditions are sometimes termed absorbing too, and also, silent, non-transmitting, non-reflecting, etc. Here, we adhere to a terminology based on whether there is a zone where the waves are forcibly absorbed (absorbing) or not (transparent).

0045-7825/$ - see front matter © 2010 Elsevier B.V. All rights reserved.
doi:10.1016/j.cma.2010.07.013

are of low-order (higher-order local conditions become more complicated). Though, local conditions are often used at truncation boundaries of heterogeneous domains without sufficient theoretical justification, the errors due to reflections are compounded.

Absorbing/layer methods typically entail surrounding a truncated finite computational domain with a layer of uniform thickness within which the waves are forced to decay. Such absorbing boundary layers presently offer the best possible alternative for domain truncation in heterogeneous domains, due, by-and-large, to the successful introduction of the perfectly-matched-layer (PML) by Bérenger in the context of electromagnetic waves [10,11]. PMLs, by construction, attenuate outwardly propagating waves without reflection from the truncation interface for all angles of incidence and frequencies. Once the waves enter the PML zone, they decay with distance according to a user-defined decay function. Although, in the continuous case, the PML can be shown to be reflection-less at the truncation interface, the spatial discretization introduces numerical reflections. However, the PML's tunable parameters enable the minimization of these reflections and allow increased accuracy even within thin layers, thereby reducing the overall computational cost. Applications of PMLs span a broad spectrum, and include, without being limited to, free-space simulation problems, radiation and scattering problems, soil–structure interaction, seismic survey problems, computational fluid dynamics, geophysical subsurface sensing, waveguides, nondestructive evaluation applications, etc.

The literature on PMLs is fairly extensive: to place in context the present development, we discuss, in chronological order, developments on PMLs, by focusing on electromagnetics, for which PMLs were first developed, and elastodynamics, which is the focus of this work. In 1994, Bérenger [10] led the way by introducing the idea of a perfectly-matched-medium in electromagnetics. Bérenger's PML was formulated based on field-splitting in order to avoid convolutional operations in the time domain, when the resulting forms are inverted back from the frequency domain. The contribution of a spatial derivative in each coordinate direction was isolated, resulting in non-physical components for each field (as the name split-field implies; the number of non-physical components equals the dimensionality of the problem). Chew and Weedon [12] suggested a reinterpretation of the PML in the context of complex-coordinate-stretching – a change of variables where spatial coordinates are mapped onto the complex space via *complex stretching functions*. Their viewpoint transformed the PML into a superior tool by endowing it with a straightforward and consistent formulation. Even though the split-field formulation doubles the number of unknowns, its remarkable absorptive performance compensated for the added cost.

However, the field-splitting alters the initial form of the system, and results in a non-Maxwellian system of equations that makes implementations into existing Maxwell-based codes difficult. An alternative (also true for elastodynamics) that maintains the original Maxwellian form of the governing equations, is to reinterpret the medium as anisotropic, while simultaneously avoiding the field-splitting, as suggested by Gedney [13]. The interpretation of PML as an artificially anisotropic material necessitated the verification of causality. Kuzuoglu and Mittra [14] claimed that the anisotropic PML is not causal, and proposed a correction by introducing a frequency-dependent real part for the stretching functions. The discussion of causality that ensued showed that Kuzuoglu and Mittra's claim was based on an error in their application of the Kramers–Krönig relationships [15]; however, their proposed correction, though not needed for causality purposes, introduced an innovative formulation of the PML, the, so-called, "complex-frequency-shifted PML" (CFS–PML). The frequency-dependent real part of the stretching functions proved onerous when inverting the resulting equations back into time domain. By means of specialized convolutional operations, the difficulty was overcome, yielding an efficient implementation of the CFS–PML in electromagnetics, referred to as "convolution PML" (CPML) [16]. The relations between the various PML formulations (up to about 2000) were nicely summarized by Texeira and Chew [17]. The equivalence between the complex-coordinate-stretching and the anisotropic formulation was shown also in [18].

Most of the PML developments are predicated upon straight-edge or planar boundaries. But for certain problems, the generalization of PML formulations to other coordinate systems is of importance. Maloney in [19] provided an extension to cylindrical coordinates, based on geometric arguments. Using the complex-coordinate-stretching viewpoint, the cartesian PML was extended to cylindrical and spherical coordinates in [20–23]. A theoretical analysis of Bérenger's system in curvilinear coordinates was performed by Collino and Monk [24], and optimal PML parameters were studied for the best computational performance in [25]. In [26], Liu and He pointed out that the straightforward extension of the original PML formulation to cylindrical coordinates (quasi-PML) was not reflection-less in cylindrical coordinates even in the continuum limit. The quasi-PML was simpler and computationally less demanding when compared to other PML implementations in cylindrical coordinates, since the same stretching functions were used in both the radial and angular directions. Later on, the same authors introduced a true PML formulation with different stretching functions for the radial and angular directions, and compared its performance against the quasi-PML [27]. A systematic derivation of the PML in curvilinear coordinates was also presented by Zhao [28]. Next, the generalization of PML to cartesian, cylindrical, and spherical coordinates was reviewed in [17]. Recently, for transient Maxwell equations, Donderici and Teixeira [29] developed a mixed finite element time-domain implementation of PML in doubly dispersive media, and in [30], a conformal PML was introduced for which the late-time stability and energy conservation properties have been verified numerically. The conformal PML allowed for a considerable reduction of buffer space by tightly circumscribing the scattering source.

Most PMLs are, by construction, excellent absorbers of propagating waves. Though evanescent waves too are absorbed efficiently [11], there is evidence that, for some frequencies, the strong attenuation might produce reflections caused by inadequately meshed PML zones [31]. In [32], Roden and Gedney showed that the CFS–PML implementation is highly absorptive of evanescent waves as well. A comparison of the split, unsplit, and CFS–PMLs revealed that split and unsplit formulations perform identically, whereas the CFS–PML forces a rapid decay of evanescent waves [33]. However, at low-frequencies, the CFS–PML suffers from degrading absorption of propagating waves. In [34], Bérenger discussed optimal CFS–PML parameters in order to absorb both evanescent and propagating waves. The CFS–PML was also effective in eliminating the observed long-time linear growth (instability) behavior of the unsplit PML [35]. Although the CFS–PML has several advantages over the standard PML, the low-frequency propagating waves are absorbed better in the standard PML. A recently developed second-order PML [36] allowed the combination of the best properties of the standard and CFS–PMLs in one PML, by simply using a stretching function that is the product of a standard and a CFS–PML stretching function. The resulting PML is as good as the CFS–PML in absorbing evanescent waves, while better attenuating the low-frequency propagating waves for waveguide problems [37]. Lou [38] presented a successful finite element time-domain implementation of this second-order PML.

Chew and Liu [39] were the first to extend the PML developments from electromagnetics to elastodynamics using a split-field, velocity–stress formulation, implemented using finite differences. Concurrently, Hastings et al. [40] developed a PML for elastic

waves using displacement potentials and a velocity–stress formulation, implemented using finite differences, which, however, could not be used in the presence of interface boundaries, such as those arising in layered media. Liu [41] introduced a PML in cylindrical and spherical coordinates in elastodynamics based on split-fields. Later on, Collino and Tsogka [42] discussed a finite difference, time-domain, velocity–stress, split-field formulation and implementation, which appears identical to Chew and Liu [39], but was also used for applications involving anisotropic media. A mixed finite element implementation of the velocity–stress split-field formulation, in the context of a fictitious domain method, was discussed by Bécache et al. [43]. All of the above key developments were based on velocity–stress schemes that are first-order in time.

In [44], Komatitsch and Tromp introduced a new split-field approach, whereby stress terms are eliminated, but the displacement field is split into four components, resulting in either third-order (in time) semi-discrete forms for the four displacement fields, or a second-order system coupled with one first-order equation for one of the displacement fields. Despite its complexity, their scheme was the first to create a displacement-only PML formulation in elastodynamics.

An unsplit-field finite difference PML formulation was introduced by Wang and Tang [45] for elastodynamics, using the recursive convolution method of CPML developed originally for electromagnetics. However, in [45], the authors used standard stretching functions for their PML implementation, by contrast to the complex-frequency-shifted stretching functions of the original CPML formulation.

In [46], Basu and Chopra developed an unsplit-field PML for time-harmonic elastodynamics and implemented it using finite elements. Shortly thereafter, they also presented the time-domain implementation, using a rather complicated time integration scheme [47]. Recently, in [48], Basu used an explicit scheme to improve on the implicit time integration scheme previously used, but, despite the computational gain, the complexity remains. In [49], Cohen and Fauqueux discussed a formulation, based on a novel decomposition of the elastodynamics equations as a first-order system, which was implemented using a mixed finite element approach and spectral elements. To arrive at the first-order decomposition, the authors split the strain tensor, and introduced independent stress variables to account for the split strain tensor components. In [50], Festa and Vilotte, also discussed mixed formulations (velocity–displacement, and velocity–stress), the use of spectral elements, and a time-staggering scheme for marching in time. Their formulation differs decidedly from Cohen and Fauqueux: the authors in [50] followed classical lines for reducing the second-order displacement-only elastodynamic problem to a first-order in time system, and used split-fields for both the velocity and stress components (as opposed to the splitting of the strain tensor).

Recently, in [51] Drossaert and Giannopoulos discussed an alternative implementation of the unsplit PML that is based on recursive integration (RIPML), rather than the explicit computation of convolutions. Later, in [52], they implemented the CPML for elastodynamics using the complex-frequency-shifted stretching functions, and reported better performance than the RIPML.

The majority of the developments in elastodynamics refer to the isotropic case. Notable exceptions include the earlier work by Collino and Tsogka [42], where they showed that the split-field standard PML can also handle heterogeneous and anisotropic media. However, the stability of the PML and the effect of anisotropy was studied later by Bécache et al. [53], where it was shown that, while the standard PML is stable for isotropic applications, it is conditionally unstable for anisotropic applications. The authors proposed necessary conditions for stability in the form of inequalities implicating the material constants. More recently, in [54], Meza-Fajardo and Papageorgiou discussed a novel PML approach, termed M-PML, which results from the introduction of coordinate-stretching and associated decay functions along all coordinate directions, that is, not only along the direction normal to the PML interface, as has been the norm to date. Their resulting split-field, non-convolutional M-PML exhibits superior performance when compared to the standard PML formulations, especially for waves propagating at grazing angles. They also showed that the M-PML is capable of handling anisotropy, without the long-time instability reported earlier for the CPML and standard PML formulations.

The performance of the PML has been investigated also for Rayleigh and interface waves [55]. It was shown that both were attenuated remarkably well. Komatitsch and Tromp [44] also confirmed the efficiency of PML in absorbing surface waves, but the performance of the discrete PML at grazing incidence was rather poor. This limitation was also reported in [51], but has been removed, owing to the CPML formulation reported by Komatitsch and Martin [56].

Any PML implementation entails user-chosen values for a number of PML parameters. There are very few comprehensive parametric studies reported in the literature that provide guidance on parameter selection. A notable exception is the work by Harari and Albocher [57], where the authors studied, using dispersion analysis, the effect of PML parameters for the time-harmonic elastic case, and presented guidelines for the proper choice of PML parameter values. Guidelines on the discretization of the PML, for any choice of the PML parameters, were also given in [58].

Table 1 summarizes the key developments to date for time-domain elastodynamics, classified depending on whether the primary unknowns are split or not, and whether the implementation is done using finite differences (FD), or finite/spectral elements (FE/SE). In general, when the PML formulation involves split-fields, almost always the resulting scheme is mixed [39–43,49,50,54], i.e., both displacements/velocities *and* stresses become unknowns. The one exception is the approach by Komatitsch and Tromp [44], where the displacement field was the only unknown, albeit split into four components. On the other hand, unsplit-field schemes require, in general, the evaluation of convolutions [45,51,52,56], which, despite the use of recursive evaluation schemes, remain expensive. One exception here is the work by Basu and Chopra [47], and by Basu [48], where the authors, though they came close to defining a mixed problem (with unsplit displacement and stresses as unknowns), they ended up departing considerably from it at the discrete level, in favor of implementing a complicated time-marching scheme. We note that, in general, the penalty one pays for a purely displacement-only formulation is an increase in the temporal complexity, which, as a result, calls for specialized time integration schemes. The temporal complexity arises from the structure of the PML, and in particular, from the

Table 1
PML implementations in time-domain elastodynamics.

	Split-field	Unsplit-field
FD	Chew and Liu [39] Hastings et al. [40] Liu [41] Collino and Tsogka [42]	Wang and Tang [45] Drossaert and Giannopoulos [51,52] Komatitsch and Martin [56]
FE/SE	Bécache et al. [43] Komatitsch and Tromp [44] Cohen and Fauqueux [49] Festa and Vilotte [50] Meza-Fajardo and Papageorgiou [54]	Basu and Chopra [47] Basu [48]

choice of the stretching function. The mixed approach relaxes the temporal complexity, and as will be shown here, leads to a second-order in time semi-discrete forms. In a recent work by Martin et al. [59], the authors presented a formulation, where the interior is treated using a standard displacement-only formulation, retaining a mixed velocity–stress form for the PML (CPML in this case), and an *ad hoc* coupling at the interface – all resolved using finite differences. Their approach reduces considerably the overall number of degrees-of-freedom, due to the non-mixed form of the interior problem.

Since most PML developments to date, including the one we will be discussing herein, lead to mixed formulations, we provide next a brief overview of mixed finite element formulations; a comprehensive review is well outside the scope of this communication. In [60] Arnold presented an outstanding introductory level discussion of mixed methods, their advantages and disadvantages, and the concepts of convergence, approximability and stability. Whereas standard single-field finite elements require approximants for a single distributed variable, mixed schemes require approximants for two (or more) fields. For stability, the choice of the approximants in mixed problems cannot be arbitrary, and must satisfy an *inf–sup* condition (also referred to as Ladyzhenskaya–Babuška–Brezzi (LBB) condition).

In an interesting review by Brezzi [61], the author pointed out that there exist two possible variational forms for treating a mixed problem such as the one arising in elasticity; the two forms result in *decidedly different* regularity requirements for the approximants. In the first form the regularity required for the stress approximants is higher than that of the displacement approximants; this is the classic mixed method. The first family of mixed finite elements related to this variational form was introduced by Raviart and Thomas for second-order elliptic problems (RT elements) [62]. Later on, several other special mixed finite elements were introduced: Johnson–Mercier [63], Brezzi–Douglas–Marini (BDM) [64], MINI element [65], PEERS (plane elasticity element with reduced symmetry) [66], etc. Other related developments can be found in [67–83].

On the other hand, in the second form, which differs from the first simply by an integration by parts, the regularity requirements are somewhat reversed: the regularity for the displacement approximants should be higher than that of the stress approximants. The latter requirements are less onerous for implementation purposes and do not require any special element types, such as the RT and BDM. In this work, we favor this second, and largely unexplored, variational form. Thus, in short, we use *unsplit fields* resulting in a *non-convolutional mixed PML*, where both displacements and stresses are treated as unknowns, and employ *finite elements* to resolve the unknowns.

To date, there are four developments that are closely related to ours, but they all differ in substantial ways: Bécache et al. [43] used a classic mixed method, but split-fields; Cohen and Fauqueux [49] used a unique mixed method, unlike any other in the literature, and split the strain tensor fields; Festa and Vilotte [50] used the same non-classic mixed method as ours, but ended up using split-fields; and finally Basu and Chopra [47] came close to casting the problem in a mixed form using unsplit fields similar to ours, but ended up with a discrete implementation that destroyed the mixed form, in favor of a complicated time-marching scheme. Their semi-discrete forms are *almost* second-order in time, but include an internal force term, whose computation requires both the storage of strains (thus, effectively, rendering the scheme mixed), as well as the temporal integration of the strains at every time step, unless, at the expense of accuracy, some form of linearization is adopted. We remark that, as is the case with any mixed form, there always results an increase in the number of unknowns, when compared to non-mixed methods. However, in light of the fact that most developments to date employ mixed split-fields, where the unknowns include the split-fields of both velocities and stresses, the form proposed herein results in computational savings, even though, when compared to interior displacement-only methods it is expensive. But, then again, displacement-only methods capable of handling arbitrary heterogeneity for infinite or semi-infinite domains, directly in the time-domain, have yet to appear.

In Section 2 we review the complex-coordinate-stretching concept; in Section 3 we obtain the two-dimensional unsplit-field PML strong form. In Section 4, we discuss the mixed finite element formulation and provide implementation details, and in Section 5, we report on numerical results demonstrating the stability and efficacy of the approach.

2. Complex-coordinate-stretching

The key idea of complex-coordinate-stretching [12,17] is a simple change of variables, where the spatial coordinates are mapped onto the complex space via complex stretching functions. The coordinate change is applied to the equations written for the frequency domain and, if required, the resulting complex-transformed equations are inverted back into the time domain. Portions of the material discussed in this section is not new (see cited references), but is provided to allow for context, completeness, and illumination of differences.

2.1. Key idea

Without reference to any specific coordinate system (the system needs to be orthogonal), let s denote the coordinate along a coordinate axis normal to the interface between the PML and the regular (interior) domain. Assuming that the interface is located at s_o, the computational domain of interest is the region $0 \leqslant s < s_o$, whereas $s_o < s \leqslant s_t$ is the PML with a layer thickness of L_{PML}, as depicted in Fig. 1.

The original coordinate variable s is replaced by the "stretched" coordinate $\tilde{s}$ in any equation s appears, where $\tilde{s}$ is defined as

$$\tilde{s} = \int_0^s \varepsilon_s(s', \omega) ds'. \tag{1}$$

In the above, ω denotes circular frequency, and ε_s is a complex stretching function in the direction of coordinate s. The standard PML results when the following form of stretching function is used (which we too adopt herein):

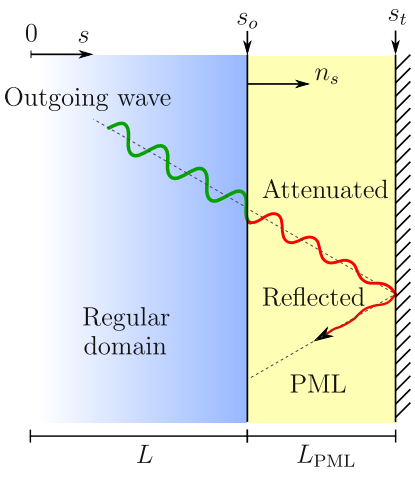

Fig. 1. A PML truncation boundary in the direction of coordinate s.

$$\varepsilon_s(s,\omega) = \alpha_s(s) + \frac{\beta_s(s)}{i\omega}, \tag{2}$$

where α_s and β_s denote scaling and attenuation functions, respectively. As the names imply, the real part α_s of ε_s "stretches" or scales s, whereas the imaginary part β_s of ε_s is responsible for the amplitude decay of the propagating wave once it enters the PML. The role of α_s is reversed in the case of evanescent waves, where it, instead of β_s, becomes responsible for their amplitude decay post-PML-entry. Specifically, for waves propagating outwardly along s, their amplitude is proportional to e^{-iks}, which, after the substitution of s by $\tilde{s}$, becomes:

$$e^{-ik\tilde{s}} = e^{-ik\int_0^s \alpha(s')ds'} e^{-\frac{k}{\omega}\int_0^s \beta(s')ds'}, \tag{3}$$

and similarly, for evanescent waves:

$$e^{-k\tilde{s}} = e^{-k\int_0^s \alpha(s')ds'} e^{\frac{ik}{\omega}\int_0^s \beta(s')ds'}. \tag{4}$$

Thus, to enforce both propagating and evanescent waves to be attenuated within the PML, we require that α_s and β_s are monotonically increasing functions of s; moreover:

$$\alpha_s(s) > 1 \quad \text{and} \quad \beta_s(s) > 0, \quad s_o < s \leqslant s_t,$$

whereas, in the regular domain we require that

$$\alpha_s(s) = 1 \quad \text{and} \quad \beta_s(s) = 0, \quad 0 \leqslant s < s_o,$$

so that $\tilde{s} \equiv s$ in the regular domain (no scaling or attenuation within the regular domain). At the interface, continuity between the two domains is maintained by setting $\alpha_s(s_o) = 1$ and $\beta_s(s_o) = 0$. The latter conditions are responsible for ensuring that the interface becomes invisible to the waves entering the PML. Since the scaling and attenuation functions do not depend on frequency, the rate of decay in the PML is frequency-independent. Although α_s is usually taken equal to one, using a value larger than one within the PML improves the attenuation of strong evanescent waves [41].

An alternative form of the stretching function was proposed by Kuzuoglu and Mittra [14], giving rise to the, so-called, frequency-shifted stretching, where

$$\varepsilon_s(s,\omega) = \alpha_s(s) + \frac{\beta_s(s)}{\kappa_s(s) + i\omega\gamma}. \tag{5}$$

Using (5) results in the CFS–PML formulation where both the real and imaginary parts of ε_s are now frequency-dependent. In transient implementations of the unsplit-field PML, the use of (5) results in convolutional operations. It has been shown that the CFS–PML outperforms the standard PML in attenuating evanescent waves, though, with a degrading absorption of low-frequency propagating waves [32–34]. In an effort to combine the best of both stretching functions, a second-order PML was introduced in [36] where

$$\varepsilon_s(s,\omega) = \left(\alpha_s(s) + \frac{\beta_s(s)}{i\omega\gamma}\right)\left(\alpha_s^*(s) + \frac{\beta_s^*(s)}{\kappa_s(s) + i\omega\gamma}\right). \tag{6}$$

Although the implementation of (6) is not trivial in the time domain, the second-order PML is the best choice when both low-frequency propagating waves and strong evanescent waves are present [37]. In this work, the stretching function defined in (2) is preferred since it leads to a straightforward implementation and exhibits better performance with low-frequency propagating waves.

Lastly, with the aid of the fundamental theorem of calculus, there also holds that

$$\frac{d\tilde{s}}{ds} = \frac{d}{ds}\int_0^s \varepsilon_s(s',\omega)ds' = \varepsilon_s(s,\omega) \Rightarrow \frac{d}{d\tilde{s}} = \frac{1}{\varepsilon_s(s,\omega)}\frac{d}{ds}. \tag{7}$$

Relation (7) will be used to transform the governing equations. For notational brevity, the functional dependence of ε_s will be henceforth omitted.

It is important to note that, by construction, the particular form of the stretching function (2) used herein clearly fails for the static case, i.e. for $\omega = 0$. Therefore, using this stretching function, one cannot obtain a PML suitable for truncating a semi-infinite domain and recover displacement and stress fields corresponding to static loading. All subsequent derivations are predicated upon the exclusion of the zero frequency from consideration.

2.2. Stretching function choice

There is no rigorous methodology suggested in the literature for choosing the scaling and attenuation functions α_s and β_s, respectively, but the key idea is to have a profile varying smoothly with distance within the PML. To minimize reflections, generally, either quadratic or linear profiles have been recommended [39]; quadratic profiles have been broadly used in elastodynamics [42,44,49,50]. A commonly adopted form of the attenuation profile, of arbitrary polynomial degree m, is

$$\beta_s(s) = \begin{cases} 0, & 0 \leqslant s \leqslant s_o, \\ \beta_o\left[\frac{(s-s_o)n_s}{L_{\text{PML}}}\right]^m, & s_o < s < s_t, \end{cases} \tag{8}$$

where β_o is a user-chosen scalar parameter, m is the degree of the polynomial attenuation, and n_s is the sth component of the outward normal to the interface between the PML and the regular domain. For ε_s to remain dimensionless, parameter β_o must have units of frequency. Based on one-dimensional wave propagation ideas, β_o can be shown to assume the form

$$\beta_o = \frac{(m+1)c_p}{2L_{\text{PML}}}\log\left(\frac{1}{|R|}\right), \tag{9}$$

where R is a user-tunable reflection coefficient controlling the amount of reflections from the outer PML boundary that is typically set as fixed, and c_p is the P-wave velocity. Once a polynomial degree is specified for the attenuation profile, the strength of decay in the PML can be tuned by controlling R.

The scaling function (α_s) controls the decay of evanescent waves and affects the performance of the PML. It is common practice to use similar profiles for both scaling and attenuation functions. Since α_s is required to be unity in the regular domain, a form similar to the attenuation profile β_s requires that α_s be expressed as

$$\alpha_s(s) = \begin{cases} 1, & 0 \leqslant s \leqslant s_o, \\ 1 + \alpha_o\left[\frac{(s-s_o)n_s}{L_{\text{PML}}}\right]^m, & s_o < s < s_t, \end{cases} \tag{10}$$

where α_o is a user-chosen dimensionless scalar parameter. To avoid having two different tuning parameters, here, we employ a form similar to β_o

$$\alpha_o = \frac{(m+1)b}{2L_{\text{PML}}}\log\left(\frac{1}{|R|}\right), \tag{11}$$

where b is a characteristic length of the domain (e.g., element size).

In this work, we favor quadratic profiles ($m = 2$), even though higher-order profiles enforce more gradual attenuation within the PML. In summary,

$$\alpha_s(s) = \begin{cases} 1, & 0 \leqslant s \leqslant s_o, \\ 1 + \frac{3b}{2L_{\text{PML}}}\log\left(\frac{1}{|R|}\right)\left[\frac{(s-s_o)n_s}{L_{\text{PML}}}\right]^2, & s_o < s < s_t, \end{cases} \tag{12a}$$

$$\beta_s(s) = \begin{cases} 0, & 0 \leqslant s \leqslant s_o, \\ \frac{3c_p}{2L_{\text{PML}}}\log\left(\frac{1}{|R|}\right)\left[\frac{(s-s_o)n_s}{L_{\text{PML}}}\right]^2, & s_o < s < s_t. \end{cases} \tag{12b}$$

We note that, in general, the polynomial order m in (8) controls the shape of the attenuation profile within the PML: depending on the order, a sharper transition could be imposed either closer

to the PML-regular domain interface, or closer to the fixed PML boundary. This, in turn, drives the meshing within the PML so that the sharper profile portion of the attenuation profile is adequately resolved. Moreover, the scalar factor in front of the polynomial term in the expression (12b) for β_s controls the intensity of the imposed attenuation: thus, the reference velocity c_p, the PML length L_{PML}, and the reflection coefficient R all play an equal role in controlling the attenuation. Herein, we use R to control the attenuation intensity, primarily due to its physical meaning.

3. Two-dimensional unsplit-field PML

In coordinate-system-independent form, the propagation of linear elastic waves is governed by the equations of motion, the generalized Hooke's law, and the kinematic conditions:

$$\mathbf{div}\ \mathcal{S}^T + \mathbf{f} = \rho\ddot{\mathbf{u}}, \tag{13a}$$

$$\mathcal{S} = \mathcal{C} : \mathcal{E}, \tag{13b}$$

$$\mathcal{E} = \frac{1}{2}[\nabla\mathbf{u} + (\nabla\mathbf{u})^T], \tag{13c}$$

where $\mathcal{S}$, $\mathcal{E}$, and $\mathcal{C}$ are the stress, strain, and elasticity tensors, respectively; ρ is the density of the elastic medium, $\mathbf{u}$ is the displacement vector, $\mathbf{f}$ is the load vector, $(:)$ denotes tensor inner product, and a dot $(\dot{})$ denotes differentiation with respect to time of the subtended function.

The PML formulation results from the application of complex coordinate-stretching to the governing equations so that the resulting system governs the motion within both the regular and PML domains. To this end, Eqs. (13a)–(13c) must first be Fourier-transformed, then stretched, and finally inverted back into the time-domain for transient implementations. Within the regular domain, the stretched equations reduce, by construction of the stretching function ε_s, to the original, undisturbed, system of governing equations.

3.1. Frequency-domain equations

First, the equilibrium, constitutive, and kinematic Eqs. (13a)–(13c) are Fourier-transformed into the frequency-domain, to obtain

$$\mathbf{div}\ \widehat{\mathcal{S}}^T + \hat{\mathbf{f}} = -\omega^2\rho\hat{\mathbf{u}}, \tag{14a}$$

$$\widehat{\mathcal{S}} = \mathcal{C} : \widehat{\mathcal{E}}, \tag{14b}$$

$$\widehat{\mathcal{E}} = \frac{1}{2}[\nabla\hat{\mathbf{u}} + (\nabla\hat{\mathbf{u}})^T], \tag{14c}$$

where a caret $(\hat{})$ denotes the Fourier transform of the subtended function. In deriving (14a), we assumed initially silent conditions for the displacement field. Moreover, implicit in the above expressions is the spatial and frequency dependence of the displacement vector, stress, and strain tensors. Next, we introduce the coordinate-stretched form for each coordinate,

$$\tilde{s} = \int_0^s \varepsilon_s(s')ds', \quad \varepsilon_s(s,\omega) = \alpha_s(s) + \frac{\beta_s(s)}{i\omega}, \quad s = x, y. \tag{15}$$

The stretching is applied first to the equations of motion (13a) by replacing x and y with the stretched coordinates $\tilde{x}$ and $\tilde{y}$; to clarify, we make use of unabridged notation:

$$\frac{\partial\hat{\sigma}_{xx}}{\partial\tilde{x}} + \frac{\partial\hat{\sigma}_{yx}}{\partial\tilde{y}} + \hat{f}_x = -\omega^2\rho\hat{u}_x, \tag{16a}$$

$$\frac{\partial\hat{\sigma}_{xy}}{\partial\tilde{x}} + \frac{\partial\hat{\sigma}_{yy}}{\partial\tilde{y}} + \hat{f}_y = -\omega^2\rho\hat{u}_y, \tag{16b}$$

where σ_{ij} denotes the stress tensor component on the plane normal to i in the direction of j ($\sigma_{ij} = (\mathcal{S})_{ij}$). Making use of (7), (16) can be written in terms of the non-stretched coordinates as

$$\frac{1}{\varepsilon_x}\frac{\partial\hat{\sigma}_{xx}}{\partial x} + \frac{1}{\varepsilon_y}\frac{\partial\hat{\sigma}_{yx}}{\partial y} + \hat{f}_x = -\omega^2\rho\hat{u}_x, \tag{17a}$$

$$\frac{1}{\varepsilon_x}\frac{\partial\hat{\sigma}_{xy}}{\partial x} + \frac{1}{\varepsilon_y}\frac{\partial\hat{\sigma}_{yy}}{\partial y} + \hat{f}_y = -\omega^2\rho\hat{u}_y. \tag{17b}$$

Next, we multiply both sides of (17) by $\varepsilon_x\varepsilon_y$; there results

$$\mathbf{div}\left(\widehat{\mathcal{S}}^T\widetilde{\Lambda}\right) + \varepsilon_x\varepsilon_y\hat{\mathbf{f}} = -\omega^2\rho\varepsilon_x\varepsilon_y\hat{\mathbf{u}}, \tag{18}$$

in which the tensor $\widetilde{\Lambda}$ is defined as (the definition is identical to that used in [47])

$$\widetilde{\Lambda} = \begin{bmatrix}\varepsilon_y & 0\\ 0 & \varepsilon_x,\end{bmatrix} = \begin{bmatrix}\alpha_y & 0\\ 0 & \alpha_x\end{bmatrix} + \frac{1}{i\omega}\begin{bmatrix}\beta_y & 0\\ 0 & \beta_x\end{bmatrix} = \widetilde{\Lambda}_e + \frac{1}{i\omega}\widetilde{\Lambda}_p, \tag{19}$$

and the subscripts "e" and "p" refer to attenuation functions associated with evanescent and propagating waves, respectively. In the regular domain, $\widetilde{\Lambda}_e$ reduces to the identity tensor, whereas $\widetilde{\Lambda}_p$ vanishes identically. After substituting (19) and (15) into (18), rearranging and grouping like-terms, there results

$$\mathbf{div}\left(\widehat{\mathcal{S}}^T\widetilde{\Lambda}_e + \frac{1}{i\omega}\widehat{\mathcal{S}}^T\widetilde{\Lambda}_p\right) + \left[a\hat{\mathbf{f}} + \frac{b}{i\omega}\hat{\mathbf{f}} + \frac{c}{(i\omega)^2}\hat{\mathbf{f}}\right] = \rho[(i\omega)^2 a\hat{\mathbf{u}} + i\omega b\hat{\mathbf{u}} + c\hat{\mathbf{u}}], \tag{20}$$

where

$$a = \alpha_x\alpha_y, \quad b = \alpha_x\beta_y + \alpha_y\beta_x, \quad c = \beta_x\beta_y. \tag{21}$$

We note that, within the regular domain, $a \equiv 1$, $b \equiv 0$, $c \equiv 0$, and since the body forces $\mathbf{f}$ are non-vanishing only within the regular domain, (20) reduces further to:

$$\mathbf{div}\left(\widehat{\mathcal{S}}^T\widetilde{\Lambda}_e + \frac{1}{i\omega}\widehat{\mathcal{S}}^T\widetilde{\Lambda}_p\right) + a\hat{\mathbf{f}} = \rho[(i\omega)^2 a\hat{\mathbf{u}} + i\omega b\hat{\mathbf{u}} + c\hat{\mathbf{u}}]. \tag{22}$$

Similarly, we apply complex-coordinate-stretching to the kinematic Eq. (14c); there results

$$\widehat{\mathcal{E}} = \frac{1}{2}\left\{(\nabla\hat{\mathbf{u}})\begin{bmatrix}\frac{1}{\varepsilon_x} & 0\\ 0 & \frac{1}{\varepsilon_y}\end{bmatrix} + \begin{bmatrix}\frac{1}{\varepsilon_x} & 0\\ 0 & \frac{1}{\varepsilon_y}\end{bmatrix}(\nabla\hat{\mathbf{u}})^T\right\} = \frac{1}{2}[(\nabla\hat{\mathbf{u}})\Lambda + \Lambda^T(\nabla\hat{\mathbf{u}})^T], \tag{23}$$

where the stretching tensor Λ is defined as

$$\Lambda = \begin{bmatrix}\frac{1}{\varepsilon_x} & 0\\ 0 & \frac{1}{\varepsilon_y}\end{bmatrix}. \tag{24}$$

Next, we pre- and post-multiply (23) by $i\omega\,\Lambda^{-T}$ and Λ^{-1} similarly to [47], respectively, to obtain

$$i\omega\Lambda^{-T}\widehat{\mathcal{E}}\Lambda^{-1} = \frac{1}{2}i\omega[\Lambda^{-T}(\nabla\hat{\mathbf{u}}) + (\nabla\hat{\mathbf{u}})^T\Lambda^{-1}], \tag{25}$$

where

$$\Lambda^{-1} = \begin{bmatrix}\varepsilon_x & 0\\ 0 & \varepsilon_y\end{bmatrix} = \begin{bmatrix}\alpha_x & 0\\ 0 & \alpha_y\end{bmatrix} + \frac{1}{i\omega}\begin{bmatrix}\beta_x & 0\\ 0 & \beta_y\end{bmatrix} = \Lambda_e + \frac{1}{i\omega}\Lambda_p. \tag{26}$$

Substituting (26) into (25), rearranging and grouping like-terms, results in

$$i\omega\Lambda_e^T\widehat{\mathcal{E}}\Lambda_e + \Lambda_e^T\widehat{\mathcal{E}}\Lambda_p + \Lambda_p^T\widehat{\mathcal{E}}\Lambda_e + \frac{1}{i\omega}\Lambda_p^T\widehat{\mathcal{E}}\Lambda_p = \frac{1}{2}\left[\Lambda_p^T(\nabla\hat{\mathbf{u}}) + (\nabla\hat{\mathbf{u}})^T\Lambda_p\right] + \frac{1}{2}i\omega\left[\Lambda_e^T(\nabla\hat{\mathbf{u}}) + (\nabla\hat{\mathbf{u}})^T\Lambda_e\right]. \tag{27}$$

Eqs. (22), (14b) and (27), constitute the stretched form of the governing frequency-domain equations. We note that the operation

in (25) is not unique; for example, one could pre-multiply (23) by $i\omega\varepsilon_x\varepsilon_y$ to obtain

$$i\omega\varepsilon_x\varepsilon_y\widehat{\mathcal{E}} = \frac{1}{2}i\omega[(\nabla\hat{\mathbf{u}})\widetilde{\Lambda} + \widetilde{\Lambda}(\nabla\hat{\mathbf{u}})^T], \tag{28}$$

where the stretching tensor $\widetilde{\Lambda}$ is defined in (19). Using the latter definition results in

$$i\omega a\widehat{\mathcal{E}} + b\widehat{\mathcal{E}} + \frac{c}{i\omega}\widehat{\mathcal{E}} = \frac{1}{2}i\omega\Big[(\nabla\hat{\mathbf{u}})\widetilde{\Lambda}_e + \widetilde{\Lambda}_e(\nabla\hat{\mathbf{u}})^T\Big] + \frac{1}{2}\Big[(\nabla\hat{\mathbf{u}})\widetilde{\Lambda}_p + \widetilde{\Lambda}_p(\nabla\hat{\mathbf{u}})^T\Big], \tag{29}$$

which differs considerably from (27). Use of (29) instead of (27) as the stretched kinematic condition entails advantages, and results in a considerably different formulation, which will be communicated in the future.

3.2. Time-domain equations

Next, we are interested in inverting the stretched frequency-domain equations back into the time-domain. To aid in the development, we make use of the following Fourier transform valid for any function $g(t)$ satisfying the usual requirements:

$$\mathcal{F}^{-1}\left[\frac{\hat{g}(\omega)}{i\omega}\right] = \int_0^t g(\tau)d\tau, \tag{30}$$

where $\mathcal{F}^{-1}$ denotes the inverse Fourier operator.[3] With the aid of (30), the inverse Fourier transforms of (22), (14b) and (27), written for both the regular and PML domains, become:

$$\mathbf{div}\left[\mathcal{S}^T\widetilde{\Lambda}_e + \left(\int_0^t \mathcal{S}^T d\tau\right)\widetilde{\Lambda}_p\right] + a\mathbf{f} = \rho(a\ddot{\mathbf{u}} + b\dot{\mathbf{u}} + c\mathbf{u}), \tag{31a}$$

$$\mathcal{S} = \mathcal{C} : \mathcal{E}, \tag{31b}$$

$$\Lambda_e^T\dot{\mathcal{E}}\Lambda_e + \Lambda_e^T\mathcal{E}\Lambda_p + \Lambda_p^T\mathcal{E}\Lambda_e + \Lambda_p^T\left(\int_0^t \mathcal{E}\,d\tau\right)\Lambda_p = \frac{1}{2}\left[\Lambda_p^T(\nabla\mathbf{u}) + (\nabla\mathbf{u})^T\Lambda_p\right] + \frac{1}{2}\left[\Lambda_e^T(\nabla\dot{\mathbf{u}}) + (\nabla\dot{\mathbf{u}})^T\Lambda_e\right]. \tag{31c}$$

Next, we introduce auxiliary variables $\mathbf{S}(\mathbf{x},t)$ and $\mathbf{E}(\mathbf{x},t)$, similar to what we had done in earlier work, e.g. [84], which physically represent stress and strain memories or histories, defined as

$$\mathbf{S}(\mathbf{x},t) = \int_0^t \mathcal{S}(\mathbf{x},\tau)\,d\tau, \quad \mathbf{E}(\mathbf{x},t) = \int_0^t \mathcal{E}(\mathbf{x},\tau)d\tau. \tag{32}$$

Clearly,

$$\dot{\mathbf{S}}(\mathbf{x},t) = \mathcal{S}(\mathbf{x},t), \tag{33a}$$

$$\ddot{\mathbf{S}}(\mathbf{x},t) = \dot{\mathcal{S}}(\mathbf{x},t), \tag{33b}$$

$$\dot{\mathbf{E}}(\mathbf{x},t) = \mathcal{E}(\mathbf{x},t), \tag{33c}$$

$$\ddot{\mathbf{E}}(\mathbf{x},t) = \dot{\mathcal{E}}(\mathbf{x},t). \tag{33d}$$

Thus, substituting (32) and (33) into (31) yields the time-domain equations of our unsplit-field PML formulation

$$\mathbf{div}\left(\dot{\mathbf{S}}^T\widetilde{\Lambda}_e + \mathbf{S}^T\widetilde{\Lambda}_p\right) + a\mathbf{f} = \rho(a\ddot{\mathbf{u}} + b\dot{\mathbf{u}} + c\mathbf{u}), \tag{34a}$$

$$\dot{\mathbf{S}} = \mathcal{C} : \dot{\mathbf{E}}, \tag{34b}$$

[3] In general, $\mathcal{F}^{-1}\left[\frac{\hat{g}(\omega)}{i\omega}\right] = \int_0^t g(\tau)\,d\tau - \pi\hat{g}(0)\delta(\omega)$, but, it can be shown that since, by construction, the overall development excludes $\omega = 0$, the inverse transform reduces to (30).

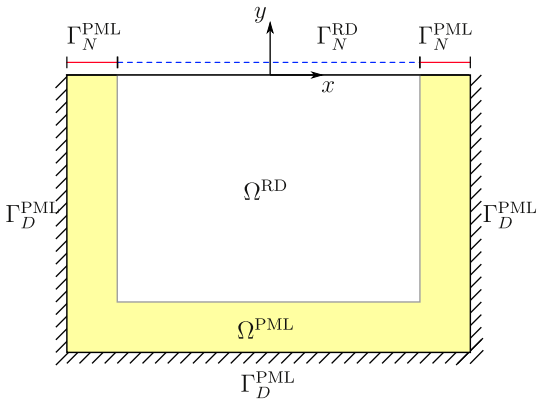

Fig. 2. A PML-truncated semi-infinite domain in two dimension.

$$\Lambda_e^T\ddot{\mathbf{E}}\Lambda_e + \Lambda_e^T\dot{\mathbf{E}}\Lambda_p + \Lambda_p^T\dot{\mathbf{E}}\Lambda_e + \Lambda_p^T\mathbf{E}\Lambda_p = \frac{1}{2}\left[\Lambda_p^T(\nabla\mathbf{u}) + (\nabla\mathbf{u})^T\Lambda_p\right] + \frac{1}{2}\left[\Lambda_e^T(\nabla\dot{\mathbf{u}}) + (\nabla\dot{\mathbf{u}})^T\Lambda_e\right]. \tag{34c}$$

4. Mixed finite element implementation

Owing to the complexity of (34), one could not conceivably reduce the set (34) to a single unknown field, as it is routinely done in displacement-based interior elastodynamics problems where there is no PML involved. Here, we propose a mixed method approach, whereby we retain both displacements and stresses (or, more appropriately, stress histories) as unknowns. To this end, we introduce the constitutive law (34b) into the kinematic condition (34c), to arrive at

$$\mathbf{div}\left(\dot{\mathbf{S}}^T\widetilde{\Lambda}_e + \mathbf{S}^T\widetilde{\Lambda}_p\right) + a\mathbf{f} = \rho(a\ddot{\mathbf{u}} + b\dot{\mathbf{u}} + c\mathbf{u}), \tag{35a}$$

$$\Lambda_e^T(\mathcal{D} : \ddot{\mathbf{S}})\Lambda_e + \Lambda_e^T(\mathcal{D} : \dot{\mathbf{S}})\Lambda_p + \Lambda_p^T(\mathcal{D} : \dot{\mathbf{S}})\Lambda_e + \Lambda_p^T(\mathcal{D} : \mathbf{S})\Lambda_p = \frac{1}{2}\left[\Lambda_p^T(\nabla\mathbf{u}) + (\nabla\mathbf{u})^T\Lambda_p\right] + \frac{1}{2}\left[\Lambda_e^T(\nabla\dot{\mathbf{u}}) + (\nabla\dot{\mathbf{u}})^T\Lambda_e\right], \tag{35b}$$

where $\mathcal{D}$ denotes the compliance tensor ($\mathbf{E} = \mathcal{D} : \mathbf{S}$). Consider next the half-plane problem depicted in Fig. 2. Let $\Omega^{\mathrm{RD}} \cup \Omega^{\mathrm{PML}} = \Omega \subset \mathbb{R}^2$ denote the region occupied by the elastic body (Ω^{RD}),[4] surrounded on three of its sides by the PML buffer zone (Ω^{PML}). Ω is bounded by $\Gamma = \Gamma_D \cup \Gamma_N$, where $\Gamma_D \cap \Gamma_N = \emptyset$, and $\Gamma_D \equiv \Gamma_D^{\mathrm{PML}}$, $\Gamma_N = \Gamma_N^{\mathrm{RD}} \cup \Gamma_N^{\mathrm{PML}}$. Moreover, let $\mathrm{J} = (0,T]$ denote the time interval of interest.

Then, we require that (35) hold in $\Omega \times \mathrm{J}$, subject to the following boundary and initial conditions:

$$\mathbf{u} = \mathbf{0} \text{ on } \Gamma_D^{\mathrm{PML}} \times \mathrm{J}, \tag{36a}$$

$$\left(\dot{\mathbf{S}}^T\widetilde{\Lambda}_e + \mathbf{S}^T\widetilde{\Lambda}_p\right)\mathbf{n} = \mathbf{0} \quad \text{on } \Gamma_N^{\mathrm{PML}} \times \mathrm{J}, \tag{36b}$$

$$\dot{\mathbf{S}}^T\mathbf{n} = \mathbf{g}_n \quad \text{on } \Gamma_N^{\mathrm{RD}} \times \mathrm{J}, \tag{36c}$$

$$\mathbf{u}(\mathbf{x},0) = \mathbf{0}, \quad \dot{\mathbf{u}}(\mathbf{x},0) = \mathbf{0} \quad \text{in } \Omega, \tag{36d}$$

$$\mathbf{S}(\mathbf{x},0) = \mathbf{0}, \quad \dot{\mathbf{S}}(\mathbf{x},0) = \mathbf{0} \quad \text{in } \Omega, \tag{36e}$$

where $\mathbf{g}_n$ denotes prescribed tractions on Γ_N^{RD}. We seek next the weak form, in the Galerkin sense, corresponding to the strong form (35–36). To this end, and for notational clarity, we introduce the symbols representing functional spaces we intend to use for scalar- (v), vector- ($\mathbf{v}$), and tensor-valued ($\mathcal{A}$) functions:

[4] RD stands for Regular Domain.

$$L^2(\Omega) = \left\{ v : \int_\Omega |v|^2 d\mathbf{x} < \infty \right\}, \tag{37a}$$

$$\mathcal{L}^2(\Omega) = \{\mathcal{A} : \mathcal{A} \in (L^2(\Omega))^{2\times 2}\}, \tag{37b}$$

$$H^1(\Omega) = \left\{ v : \int_\Omega (|v|^2 + |\nabla v|^2) d\mathbf{x} < \infty \right\}, \tag{37c}$$

$$\mathbf{H}^1(\Omega) = \{\mathbf{v} : \mathbf{v} \in (H^1(\Omega))^2\}. \tag{37d}$$

As discussed in the introduction, there are two possible variational forms one could derive for the mixed problem at hand. The only difference between the two possible formulations arises from the judicious application of integration by parts, which results in distinctly different regularity requirements for the test and trial functions between the two formulations [61]. We take inner products of the Eq. (35) with test functions $\mathbf{w}(\mathbf{x})$ and $\mathbf{T}(\mathbf{x})$, respectively, residing in appropriate spaces, and then integrate over the entire computational domain Ω. In a first variational form, the equilibrium equation (35a) is not operated on by integration by parts, whereas (35b) is. By contrast, in a second variational form, integration by parts is applied to the equilibrium Eq. (35a). Here, we prefer the latter approach, since it requires less regularity on the stresses. Thus, the weak form of (35) can be stated as: find $\mathbf{u} \in \mathbf{H}^1(\Omega) \times \mathsf{J}$ satisfying $\mathbf{u}|_{\Gamma_D^{\mathrm{PML}}} = \mathbf{0}$, and $\mathbf{S} \in \mathcal{L}^2(\Omega) \times \mathsf{J}$, such that the following equations are satisfied for all $\mathbf{w} \in \mathbf{H}^1(\Omega)$ satisfying $\mathbf{w}|_{\Gamma_D} = \mathbf{0}$ and $\mathbf{T} \in \mathcal{L}^2(\Omega)$:

$$\begin{aligned} &\int_\Omega \nabla \mathbf{w} : \left(\dot{\mathbf{S}}^T \widetilde{\Lambda}_e + \mathbf{S}^T \widetilde{\Lambda}_p \right) d\Omega + \int_\Omega \mathbf{w} \cdot \rho(a\ddot{\mathbf{u}} + b\dot{\mathbf{u}} + c\mathbf{u})\, d\Omega \\ &\qquad = \int_{\Gamma_N} \mathbf{w} \cdot \left(\dot{\mathbf{S}}^T \widetilde{\Lambda}_e + \mathbf{S}^T \widetilde{\Lambda}_p \right) \mathbf{n}\, d\Gamma + \int_\Omega \mathbf{w} \cdot a\mathbf{f}\, d\Omega, \end{aligned} \tag{38a}$$

$$\begin{aligned} &\int_\Omega (\mathcal{D} : \ddot{\mathbf{S}}) : \Lambda_e \mathbf{T} \Lambda_e^T\, d\Omega + \int_\Omega (\mathcal{D} : \dot{\mathbf{S}}) : \left(\Lambda_e \mathbf{T} \Lambda_p^T + \Lambda_p \mathbf{T} \Lambda_e^T \right) d\Omega \\ &\quad + \int_\Omega (\mathcal{D} : \mathbf{S}) : \Lambda_p \mathbf{T} \Lambda_p^T\, d\Omega \\ &\quad = \int_\Omega \nabla \mathbf{u} : \Lambda_p \mathbf{T}_{sym}\, d\Omega + \int_\Omega \nabla \dot{\mathbf{u}} : \Lambda_e \mathbf{T}_{sym}\, d\Omega, \end{aligned} \tag{38b}$$

where $\mathbf{T}_{sym}$ is the symmetric part of $\mathbf{T}$. It is important to notice that the regularity required for the stresses is *lower* than that of the displacements. For the mixed finite element implementation of the variational form (38), both $\mathbf{u}(\mathbf{x},t)$ and $\mathbf{S}(\mathbf{x},t)$ are treated as independent variables that need to be approximated separately. We introduce

$$\Xi_r^h = \{\mathbf{q} \in \mathbf{H}^1(\Omega), \quad \mathbf{q}|_K \in (Q_r(K))^2, \ \forall K \in \mathcal{K}_h\}, \tag{39a}$$

$$\Upsilon_r^h = \{\mathcal{A} \in \mathcal{L}^2(\Omega), \quad \mathcal{A}|_K \in (Q_r(K))^{2\times 2}, \ \forall K \in \mathcal{K}_h\}, \tag{39b}$$

where $Q_r(K)$ is a polynomial of degree at most r on K. $\mathcal{K}_h$ is a partition of Ω into non-overlapping *triangles* or *quadrilaterals*. Note that $\Xi_r^h \subset \mathbf{H}^1(\Omega)$ and $\Upsilon_r^h \subset \mathcal{L}^2(\Omega)$. Let the basis functions in Ξ_r^h and Υ_r^h be denoted by $\mathbf{\Phi}$ and $\mathbf{\Psi}$, respectively. The trial functions $\mathbf{u}_h \in \Xi_r^h \times \mathsf{J}$ and $\mathbf{S}_h \in \Upsilon_r^h \times \mathsf{J}$ are spatially discretized as

$$\mathbf{u}(\mathbf{x},t) \cong \mathbf{u}_h(\mathbf{x},t) = \begin{bmatrix} \mathbf{\Phi}^T(\mathbf{x})\mathbf{u}_x(t) \\ \mathbf{\Phi}^T(\mathbf{x})\mathbf{u}_y(t) \end{bmatrix}, \tag{40a}$$

$$\mathbf{S}(\mathbf{x},t) \cong \mathbf{S}_h(\mathbf{x},t) = \begin{bmatrix} \mathbf{\Psi}^T(\mathbf{x})\mathbf{S}_{xx}(t) & \mathbf{\Psi}^T(\mathbf{x})\mathbf{S}_{xy}(t) \\ \mathbf{\Psi}^T(\mathbf{x})\mathbf{S}_{yx}(t) & \mathbf{\Psi}^T(\mathbf{x})\mathbf{S}_{yy}(t) \end{bmatrix}. \tag{40b}$$

Similarly, the test functions $\mathbf{w} \in \Xi_r^h$ and $\mathbf{T} \in \Upsilon_r^h$ are expressed as

$$\mathbf{w}(\mathbf{x}) \cong \mathbf{w}_h(\mathbf{x}) = \begin{bmatrix} \mathbf{w}_x^T \mathbf{\Phi}(\mathbf{x}) \\ \mathbf{w}_y^T \mathbf{\Phi}(\mathbf{x}) \end{bmatrix}, \tag{41a}$$

$$\mathbf{T}(\mathbf{x}) \cong \mathbf{T}_h(\mathbf{x}) = \begin{bmatrix} \mathbf{T}_{xx}^T \mathbf{\Psi}(\mathbf{x}) & \mathbf{T}_{xy}^T \mathbf{\Psi}(\mathbf{x}) \\ \mathbf{T}_{yx}^T \mathbf{\Psi}(\mathbf{x}) & \mathbf{T}_{yy}^T \mathbf{\Psi}(\mathbf{x}) \end{bmatrix}. \tag{41b}$$

To reduce notational congestion, we henceforth drop the time and space dependencies. By introducing the symmetry of stress tensor ($\mathcal{S} = \mathcal{S}^T$), we obtain the following *semi-discrete form*

$$\mathbf{M}\ddot{\mathbf{U}} + \mathbf{C}\dot{\mathbf{U}} + \mathbf{K}\mathbf{U} = \mathbf{F}, \tag{42}$$

where the system matrices $\mathbf{M}$, $\mathbf{C}$, $\mathbf{K}$, and the system vectors $\mathbf{U}$ and $\mathbf{F}$ are defined as

$$\mathbf{M} = \begin{bmatrix} \mathbf{M}_a & \mathbf{0} & \mathbf{0} & \mathbf{0} & \mathbf{0} \\ \mathbf{0} & \mathbf{M}_a & \mathbf{0} & \mathbf{0} & \mathbf{0} \\ \mathbf{0} & \mathbf{0} & \mathbf{N}_{e1e1} & -\mathbf{Z}_{e1e1} & \mathbf{0} \\ \mathbf{0} & \mathbf{0} & -\mathbf{Z}_{e2e2} & \mathbf{N}_{e2e2} & \mathbf{0} \\ \mathbf{0} & \mathbf{0} & \mathbf{0} & \mathbf{0} & \mathbf{G}_{e1e2} \end{bmatrix}, \tag{43a}$$

$$\mathbf{C} = \begin{bmatrix} \mathbf{M}_b & \mathbf{0} & \mathbf{A}_{e1x} & \mathbf{0} & \mathbf{A}_{e2y} \\ \mathbf{0} & \mathbf{M}_b & \mathbf{0} & \mathbf{A}_{e2y} & \mathbf{A}_{e1x} \\ -\mathbf{B}_{e1x} & \mathbf{0} & 2\mathbf{N}_{e1p1} & -2\mathbf{Z}_{e1p1} & \mathbf{0} \\ \mathbf{0} & -\mathbf{B}_{e2y} & -2\mathbf{Z}_{e2p2} & 2\mathbf{N}_{e2p2} & \mathbf{0} \\ -\mathbf{B}_{e1y} & -\mathbf{B}_{e2x} & \mathbf{0} & \mathbf{0} & (\mathbf{G}_{e1p2} + \mathbf{G}_{p1e2}) \end{bmatrix}, \tag{43b}$$

$$\mathbf{K} = \begin{bmatrix} \mathbf{M}_c & \mathbf{0} & \mathbf{A}_{p1x} & \mathbf{0} & \mathbf{A}_{p2y} \\ \mathbf{0} & \mathbf{M}_c & \mathbf{0} & \mathbf{A}_{p2y} & \mathbf{A}_{p1x} \\ -\mathbf{B}_{p1x} & \mathbf{0} & \mathbf{N}_{p1p1} & -\mathbf{Z}_{p1p1} & \mathbf{0} \\ \mathbf{0} & -\mathbf{B}_{p2y} & -\mathbf{Z}_{p2p2} & \mathbf{N}_{p2p2} & \mathbf{0} \\ -\mathbf{B}_{p1y} & -\mathbf{B}_{p2x} & \mathbf{0} & \mathbf{0} & \mathbf{G}_{p1p2} \end{bmatrix}, \tag{43c}$$

$$\mathbf{U} = [\mathbf{u}_x \ \mathbf{u}_y \ \mathbf{S}_{xx} \ \mathbf{S}_{yy} \ \mathbf{S}_{xy}]^T, \tag{43d}$$

$$\mathbf{F} = \left[\mathbf{f}_x^{\mathbf{e}} \ \mathbf{f}_y^{\mathbf{e}} \ \mathbf{0} \ \mathbf{0} \ \mathbf{0} \right]^T, \tag{43e}$$

where

$$\mathbf{f}_x^{\mathbf{e}} = \int_{\Gamma_N^{RD}} \mathbf{\Phi} g_x(\mathbf{x},t) d\Gamma + \int_\Omega \mathbf{\Phi} a f_x\, d\Omega, \tag{44a}$$

$$\mathbf{f}_y^{\mathbf{e}} = \int_{\Gamma_N^{RD}} \mathbf{\Phi}\ g_y(\mathbf{x},t) d\Gamma + \int_\Omega \mathbf{\Phi} a f_y\, d\Omega, \tag{44b}$$

and

$$\mathbf{A}_{ijk} = \int_\Omega \widetilde{\Lambda}_i^j \frac{\partial \mathbf{\Phi}}{\partial k} \mathbf{\Psi}^T\, d\Omega, \quad \mathbf{N}_{ijkl} = \int_\Omega (1-\nu^2) \frac{\Lambda_i^j \Lambda_k^l}{E} \mathbf{\Psi}\mathbf{\Psi}^T\, d\Omega, \tag{45a}$$

$$\mathbf{B}_{ijk} = \int_\Omega \Lambda_i^j \mathbf{\Psi} \frac{\partial \mathbf{\Phi}^T}{\partial k}\, d\Omega, \quad \mathbf{Z}_{ijkl} = \int_\Omega \nu(1+\nu) \frac{\Lambda_i^j \Lambda_k^l}{E} \mathbf{\Psi}\mathbf{\Psi}^T\, d\Omega, \tag{45b}$$

$$\mathbf{M}_k = \int_\Omega k\rho \mathbf{\Phi}\mathbf{\Phi}^T\, d\Omega, \quad \mathbf{G}_{ijkl} = \int_\Omega 2(1+\nu) \frac{\Lambda_i^j \Lambda_k^l}{E} \mathbf{\Psi}\mathbf{\Psi}^T\, d\Omega, \tag{45c}$$

where E and ν above denote Young's modulus and Poisson's ratio, respectively. Note that Λ^n and $\widetilde{\Lambda}^n$ denote the nth component of the diagonal matrices Λ and $\widetilde{\Lambda}$, respectively.

We remark that the obtained semi-discrete form (42) or (43) is second-order in time. To resolve the time integration we employ a standard Newmark-β scheme. The symmetry of the mass-like, stiffness-like, and damping-like matrices in (43) has been sacrificed owing to the mixed formulation. Though the additional unknowns seem to increase the computational cost, our mixed unsplit-field formulation requires less unknowns when compared to most mixed split-field formulations.

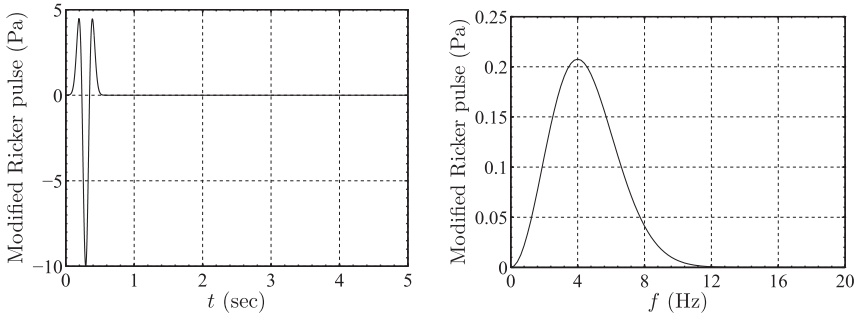

Fig. 3. Excitation time signal and its Fourier spectrum.

5. Numerical results

To test the accuracy and efficiency of our mixed unsplit-field PML formulation, we discuss next five numerical experiments, involving both homogeneous and arbitrarily heterogeneous hosts. The first example is the simplest: it involves an explosive wave source within a homogeneous semi-infinite domain. Examples 2 and 3 involve elongated domains with near-bottom-PML and near-surface wave sources, respectively, that give rise to waves incident at grazing angles, and often result in degrading PML performance [56,51,52]. The final two examples, Examples 4 and 5, focus on the implications of heterogeneity, one involving a horizontally-layered medium, and the last one involving an arbitrarily heterogeneous profile.

Beyond comparisons of time histories at select target locations, as a measure of PML performance we also provide plots of relative time-dependent errors. To obtain these relative errors, we create reference solutions by embedding the computational domain of interest Ω^{RD} within an enlarged domain Ω^{ED} with fixed exterior boundaries. The numerical solution within Ω^{ED} is obtained using a displacement-based formulation, in order to create a solution that is completely independent from the mixed approach discussed herein. We retain the enlarged domain's solution up to times that are prior to the arrival of any waves to Ω^{RD} from the part of the domain that is exterior to Ω^{RD}. We compare the reference and the mixed method solutions only within the regular domain Ω^{RD} ($\subset\Omega^{\mathrm{ED}}$). To define the error metrics, we introduce first the time-dependent L^2 norm of the displacement field over an arbitrary domain Ω as

$$D(t;\Omega)=\left[\int_{\Omega}\mathbf{u}^T(\mathbf{x},t)\mathbf{u}(\mathbf{x},t)\,d\Omega\right]^{\frac{1}{2}}. \tag{46}$$

We define the time-dependent relative error metric $e(t)$ in terms of an L^2 norm, normalized with respect to the peak value of the aforementioned displacement field norm D, as

$$e(t)=\frac{\left\{\int_{\Omega^{\mathrm{RD}}}[\mathbf{u}(\mathbf{x},t)-\mathbf{u}_{\mathrm{ED}}(\mathbf{x},t)]^T[\mathbf{u}(\mathbf{x},t)-\mathbf{u}_{\mathrm{ED}}(\mathbf{x},t)]\,d\Omega^{\mathrm{RD}}\right\}^{\frac{1}{2}}}{\max_t D(t;\Omega^{\mathrm{RD}})}\times 100. \tag{47}$$

As an additional performance metric, we also study the decay of the total energy within the regular domain, along lines similar to the ones discussed by Komatitsch and Martin [56]. In short, the energy, injected to the domain via the loading, is carried by waves that are absorbed and attenuated within the PML, and, thus, a rapid decay should be expected if the PML is working correctly. The total energy of the system as a function of time is expressed as

$$E_t(t)=\frac{1}{2}\int_{\Omega}\rho(\mathbf{x},t)\left[\dot{\mathbf{u}}^T(\mathbf{x},t)\dot{\mathbf{u}}(\mathbf{x},t)\right]d\Omega+\frac{1}{2}\times\int_{\Omega}[\boldsymbol{\sigma}^T(\mathbf{x},t)\boldsymbol{\epsilon}(\mathbf{x},t)]\,d\Omega, \tag{48}$$

where $\dot{\mathbf{u}}$, $\boldsymbol{\sigma}$, and $\boldsymbol{\epsilon}$ are velocity, stress, and strain vectors, respectively. Similarly to $e(t)$, the total energy too is computed only within the regular domain Ω^{RD}.

5.1. Homogeneous media

We consider first a homogeneous half-plane with density $\rho=2200\ \mathrm{kg/m^3}$, shear-wave velocity $c_s\simeq 5.81$ m/s, and Poisson ratio $\nu=0.2$.[5] We use an explosive P-wave source defined as

$$\mathbf{f}(\mathbf{x},t)=\mathbf{T}_{\mathrm{p}}(t)\mathbf{S}_{\mathrm{p}}(r), \tag{49}$$

where $\mathbf{T}_{\mathrm{p}}$ and $\mathbf{S}_{\mathrm{p}}$ denote the temporal and spatial parts of the loading, respectively. The spatial part is a radial function defined as

$$\mathbf{S}_{\mathrm{p}}(r)=\begin{cases}\left(1-\frac{r^2}{r_d^2}\right)^3\left(\frac{x-x_c}{r},\frac{y-y_c}{r}\right), & (x,y)\in D_0,\\ 0, & (x,y)\notin D_0,\end{cases} \tag{50}$$

where $r=\sqrt{(x-x_c)^2+(y-y_c)^2}$, and D_0 denotes the source disk of center (x_c,y_c) and radius r_d. For the temporal variation of the load we use a modified Ricker pulse defined as

$$\mathbf{T}_{\mathrm{p}}(t)=\frac{(0.25u^2-0.5)e^{-0.25u^2}-13e^{-13.5}}{0.5+13e^{-13.5}}\quad\text{with } 0\leqslant t\leqslant\frac{6\sqrt{6}}{\omega_r}, \tag{51}$$

where

$$u=\omega_r t-3\sqrt{6}, \tag{52}$$

and ω_r denotes the characteristic central circular frequency ($=2\pi f_r$) of the pulse.

In the simulations, we used a Ricker wavelet with a central frequency $f_r=4$ Hz, and a peak amplitude of 10 Pa, as depicted in Fig. 3. The explosive source radius r_d was set to 0.4 m.

Example 1. We reduced, through truncation, a semi-infinite domain to a 10 m × 10 m computational domain, surrounded on its sides and bottom by a 1 m-thick PML, as shown in Fig. 4. The explosive source disk's center was placed at 5 m below the surface, at the center of the domain. The PML and regular domains were discretized by quadratic elements with an element size of 0.1 m, whereas the disk was meshed with 0.05 m quadratic elements. The discretization resulted in a 10-cell-thick PML. The reflection coefficient R was set to 10^{-8}. Using a time step of 0.0002 s, we let the simulation run for 10 s. The time histories of the displacements and stress components are sampled at five locations sp_i, $i=1,\ldots,5$.

In order to assess the validity of our mixed PML formulation, the displacement time histories at the sampling points were compared against the response obtained using an enlarged domain with fixed

[5] We have used, by design and without loss of generality, low velocities to allow for clearer separation of the propagating waves and their reflections.

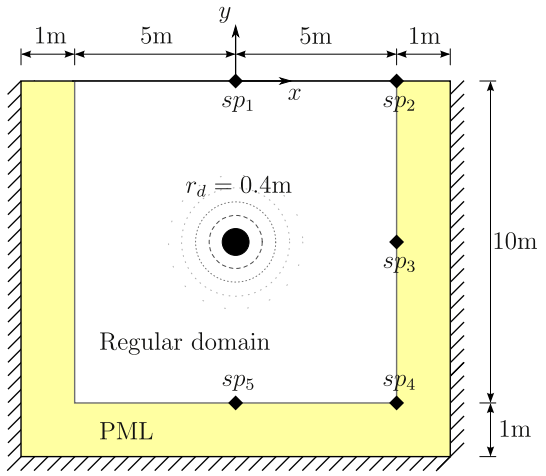

Fig. 4. A PML-truncated semi-infinite domain in two dimensions subjected to an explosive load at the domain center.

boundaries and a classical displacement-based plane-strain formulation. The enlarged domain's size (110 m × 60 m) was defined such that, during the specified time interval of interest, reflections from its fixed exterior boundaries do not travel back and interfere with the wave motion in the computational domain of interest. Fig. 5 depicts the comparison of the response time histories for u_x and u_y at the various sp_i points. As it can be seen, the agreement is excellent: the PML has effectively absorbed the waves without any reflections. It is apparent from the figures that causality holds (sometimes an issue with PML implementations), and that the response is free of spurious reflections. No numerical instabilities were observed during the total simulation time of 10 s (only half the record is shown here), i.e., for 50,000 time steps.

Fig. 6 shows snapshots of the displacements and stresses taken at two different times: the left column corresponds to, approximately, 0.2 s after the wave has impinged upon the free surface, and has also entered the side and bottom-PML zones, shown in the figure with solid black lines that are indented with respect to the outer boundary. Notice that there are reflections from the free surface as expected (e.g. local doubling of the displacement amplitudes), and contrast them against the reflection-less side and bottom-PML interfaces. The right column corresponds to a later time and clearly shows two wave trains traveling towards the bottom: each wave train features three zones, with each zone corresponding to the amplitude peaks of the Ricker wavelet. Both wave trains (one P and one S) are reflections from the free surface. Again, notice that there are no discernible reflections from the PML interfaces, nor any residual reflections from the fixed external boundaries that could have polluted the interior wave solution.

Fig. 7 depicts three different error metrics: Fig. 7(a) shows a visual comparison, displaying excellent agreement, between the reference solution and the PML-based solution for the displacement norm defined in (46); Fig. 7(b) shows the error norm defined in (47), which, at all times, is below 0.22%. Fig. 7(c) and (d) show the absolute value of the error at two distinct locations, normalized with respect to the absolute value of the peak record value; the error remains below 0.43% at all times.

Next, we study the effect the reflection coefficient R has on the quality of the obtained solutions. To this end, R was varied from 10^{-1} to 10^{-8}, in multiples of 10, and the total energy decay (48) was computed for each one of the R values, as a function of time.

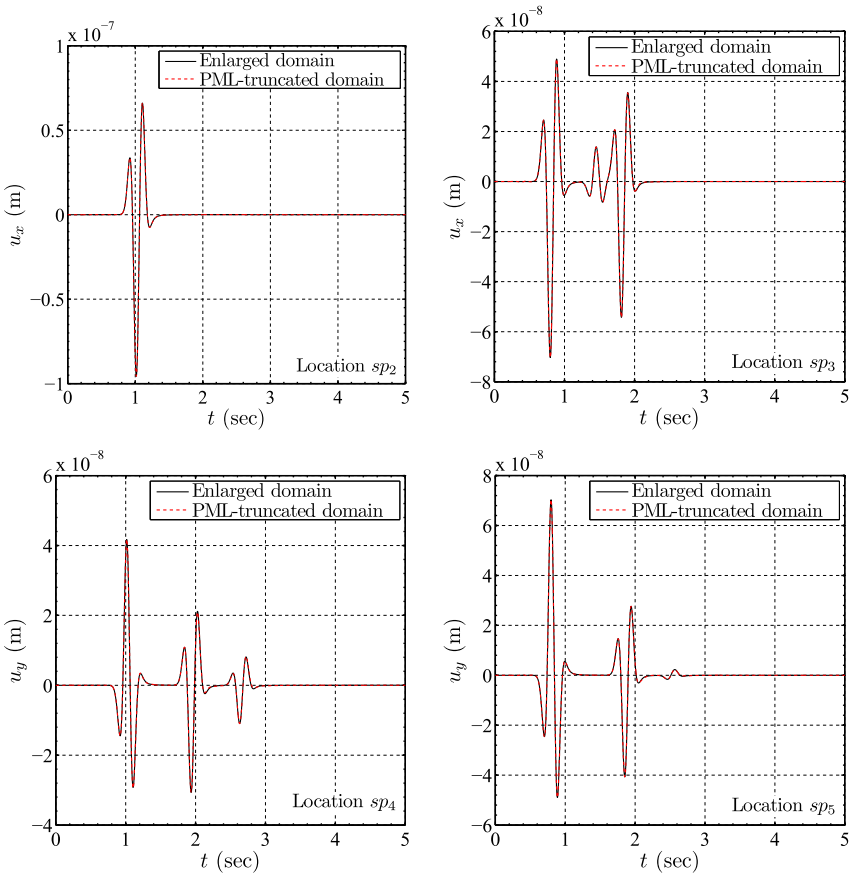

Fig. 5. Comparison of u_x and u_y time histories between the enlarged and PML-truncated domain solutions at various sampling points (Example 1).

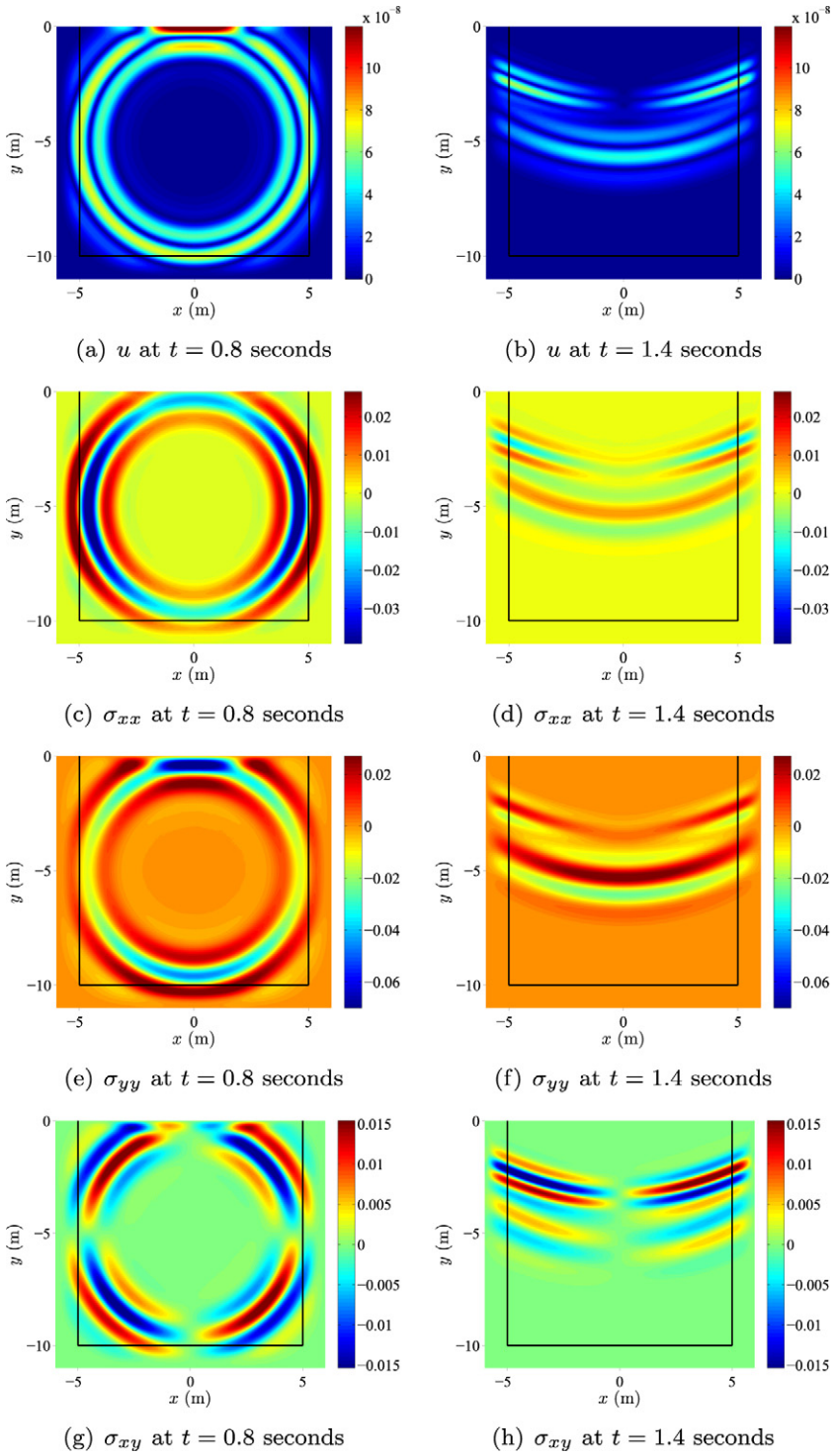

Fig. 6. Snapshots of u, σ_{xx}, σ_{yy}, and σ_{xy} using an explosive Ricker pulse source at the center of the domain.

Fig. 8 shows the energy decay plotted in standard (left), and semi-log scale (right), the former terminated at 5 s, the latter terminated at 10 s. Shown on the same figure is the energy decay for all tested R values, as well as the reference decay corresponding to the enlarged domain (recall that this has been obtained using an independent displacement-based formulation). The figure is quite revealing in several ways. First, almost all R values (except for $R = 10^{-1}$) result in similarly sharp decay: after about 2.8 s, there is hardly any discernible residual energy left in the domain, since all the waves have traveled out of the domain and have been absorbed by the PML. A closer look, using the semi-log scale, reveals though that R plays a key role in determining the rate the energy decays, with lower R values enforcing more rapid decay. As R increases, the fixed exterior PML boundaries reflect back waves of higher amplitude than those that would have resulted from lower R reflection coefficients, first within the PML and later within the regular domain. Though still of small amplitude, when compared to the peak amplitudes observed in the regular domain, the reflections become amplified as they travel back into the regular domain (this is so by construction), and stand to pollute the solution and

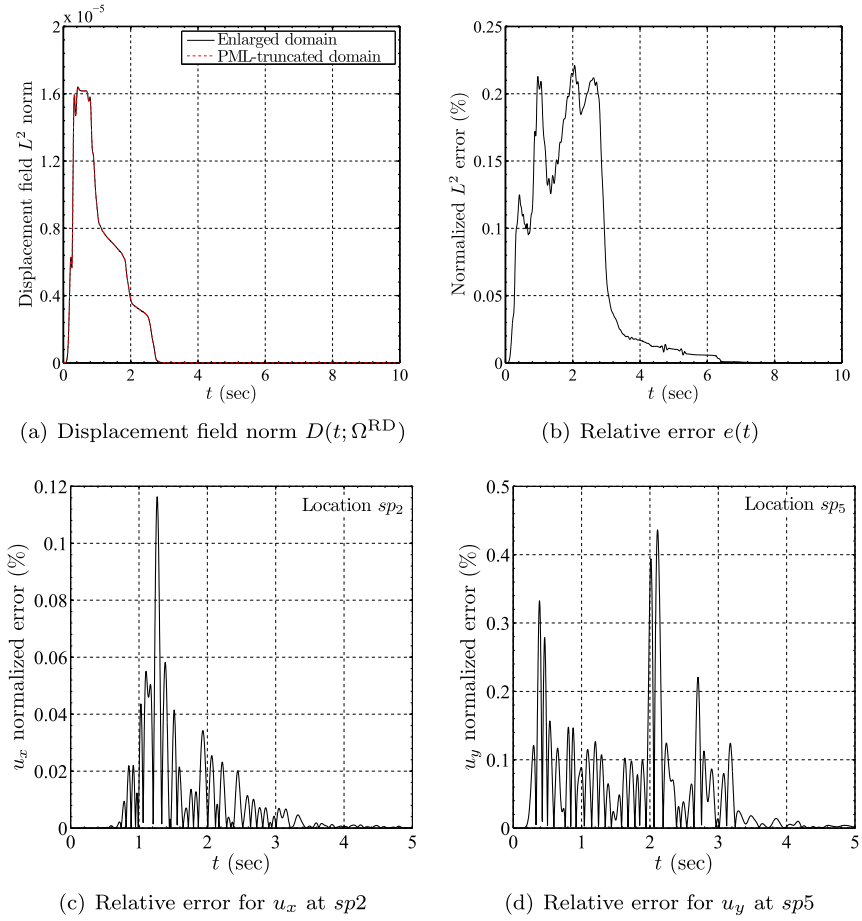

(a) Displacement field norm $D(t;\Omega^{\mathrm{RD}})$ (b) Relative error $e(t)$

(c) Relative error for u_x at $sp2$ (d) Relative error for u_y at $sp5$

Fig. 7. Error metrics for the homogeneous domain excited by an explosive Ricker pulse ($f_r = 4$ Hz) at the center of the domain (Example 1).

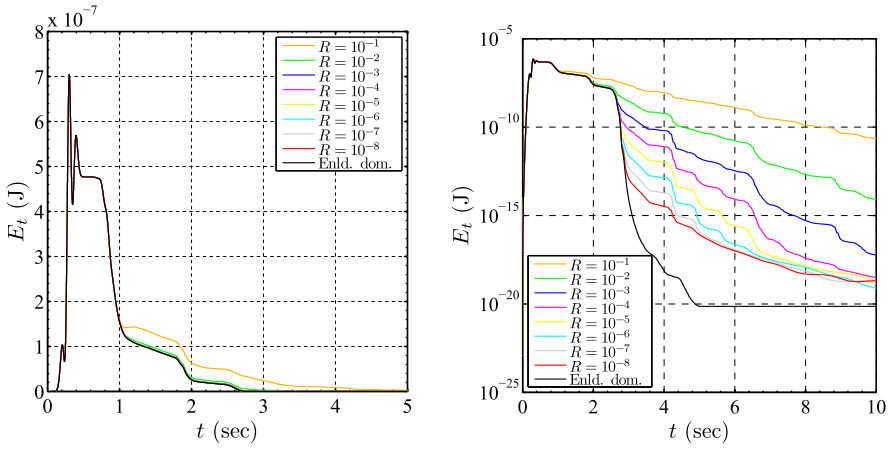

(a) Energy decay - standard scale (b) Energy decay - logarithmic scale

Fig. 8. Total energy decay inside the regular domain (Example 1).

slow the energy decay. Thus, lower R values effectively decrease the absorptive capacity of the PML layer.

Secondly, it is worth noting a few characteristic points on the energy plots: first, notice on the left plot that the energy, initially, follows closely the maxima and minima of the Ricker wavelet. At about $t = 0.5$ s the P-wave fronts have reached the free surface and the side and bottom PMLs; the first peak of the Ricker wavelet enters the PMLs at about $t = 0.7$ s, and the second and largest peak at about $t = 0.8$ s, where there is a clear change in the slope of the energy decay curve (left plot). At about $t = 1$ s the last Ricker wavelet peak has been absorbed within the 3 PML zones, and the only remaining energy within the domain is associated with the surface reflections of the original waves (both P and S). Between $t = 1.7$ s and $t = 1.9$ s the reflections' P-train peaks arrive at the bottom PML and get absorbed, whereas between, approximately, $t = 2.3$ s and $t = 2.5$ s the reflections' S-train peaks arrive at the bottom

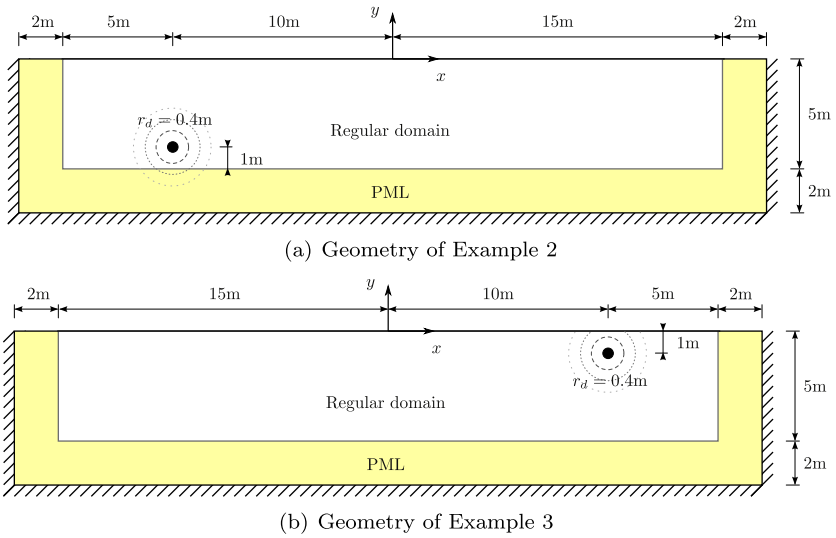

Fig. 9. Elongated PML-truncated semi-infinite domains in two dimension subjected to an explosive load.

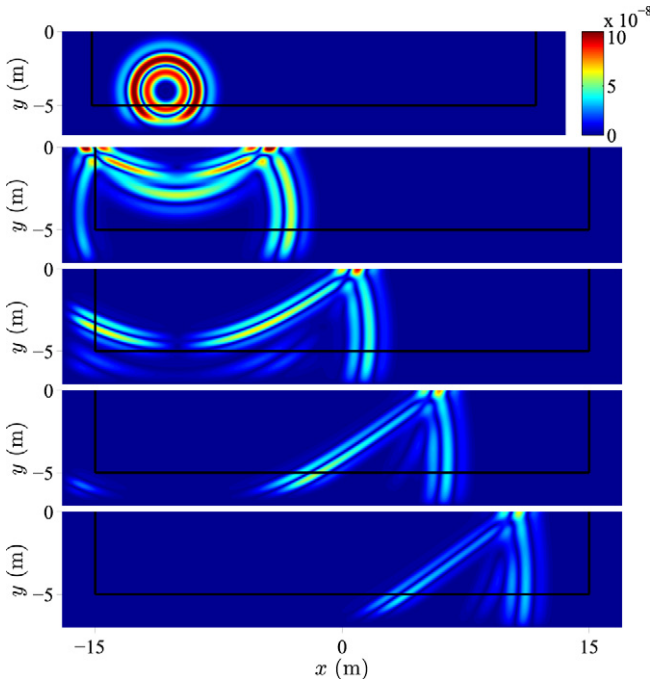

Fig. 10. Snapshots of u taken at $t = 0.5, 1.0, 1.5, 2.0, 2.5$ s in Example 2, driven by an explosive Ricker wavelet source positioned close to the bottom PML.

PML. The above result in slope changes in the energy decay curve, which can be seen in Fig. 8; by about $t = 2.8$ s all waves have left the domain.

The energy plot seems to suggest that it is always beneficial to reduce the R coefficient to as small a value as the machine accuracy may permit. However, lower R values introduce sharper PML decay profiles, as it can also be deduced from (12). That is, in sharper profiles, most of the wave absorption takes place within a small fraction of the PML length, right next to the PML-regular domain interface. For the absorption to be effective, it is critical that the mesh density within the PML adequately captures the sharp profile, to avoid the accumulation of numerical errors (the situation is similar to the difficulties arising when one attempts to approximate stress singularities with regular and inadequately sized isoparametric elements). In fact, sharper profiles are not only introduced by lower R coefficients, but arise also when *lower* polynomial degrees (m in (8)) are chosen, or when *higher* reference velocities are prescribed within the PML (c_p in (12)). Though a detailed discussion and the necessary parametric study escapes the scope of this article, we remark that we have found linear profiles to be very sharp and should, in general, be avoided, in favor of, at least, quadratic, or preferably, quartic profiles.

Notice, lastly, that for R values lower than about 10^{-6} the remaining domain energy is lower than 10^{-12}, or roughly more than five orders of magnitude less than the peak domain energy, betraying effective wave absorption.

Example 2. Since, by construction, the PML enforces attenuation only in the direction normal to the PML-regular domain interface, difficulties may arise in simulations of wave motion within elongated domains, where waves may impinge at grazing angles upon the PML interface. The PML will not attenuate waves traveling parallel to the interface, and depending on the ability of the PML mesh to adequately resolve the non-attenuated propagating waves within the PML, the solution in the regular domain stands to be polluted. Such difficulties were reported for the regularly stretched split-field PML in [51,52], and resulted in the authors' favoring of an unsplit convolutional CFS–PML. Concurrently, in [56] the authors verified the same findings when they utilized the regularly stretched split-field PML formulation of Collino and Tsogka [42]. However, in our own simulations with the unsplit-field mixed PML we have not observed such difficulties; while the mixed formulation does have an advantage, we do not believe that the mixed formulation alone is responsible for the lack of spurious reflections. Rather, we iterate that, in our experience, the PML's mesh density is critical in the generation of spurious wave motion, especially in the presence of sharp decay profiles. Again, a careful examination of the relations between attenuation function parameters (degree of polynomial m, parameter β_o) resolves the contradiction. Since β_o is generally defined to be a function of a reference P-wave velocity c_p, the reflection coefficient R, and the degree of polynomial m, these parameters cannot be arbitrarily chosen, if a gradual imposition of attenuation is to be attained. Increasing the P-wave velocity c_p, lowering the polynomial order m, or decreasing the reflection coefficient R results in sharper attenuation profiles. The faster decay necessitates more elements within the PML to properly sample the sharply-imposed

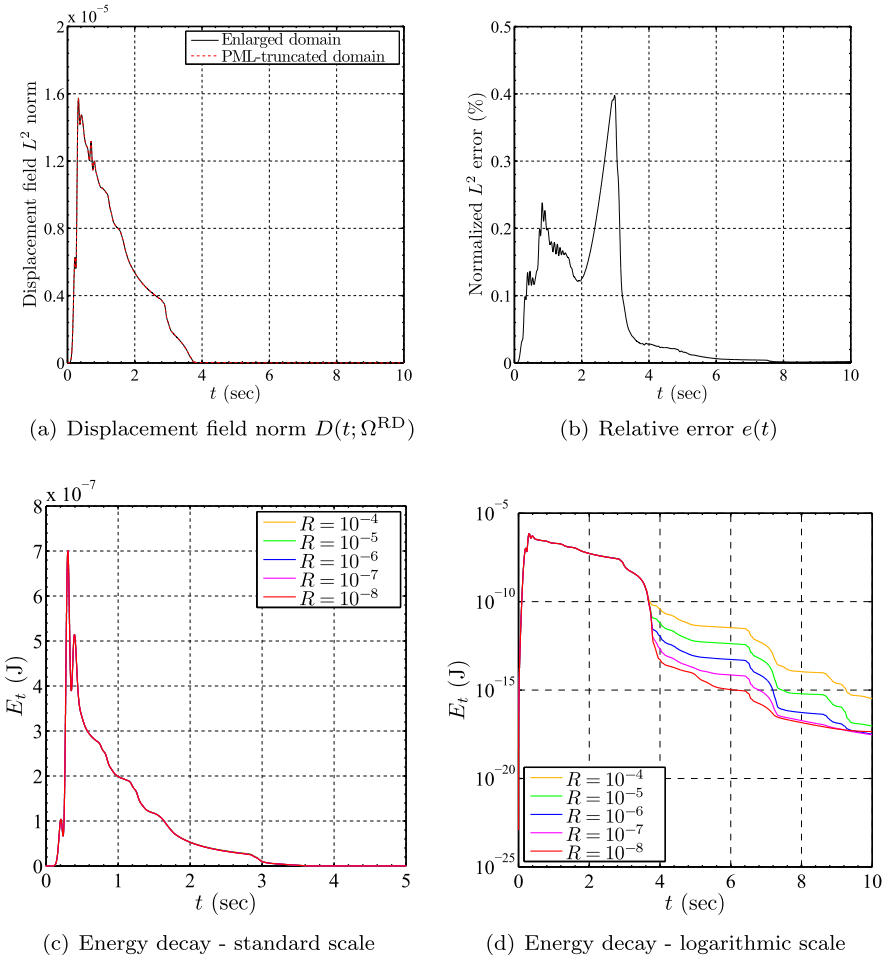

(a) Displacement field norm $D(t;\Omega^{\mathrm{RD}})$ (b) Relative error $e(t)$

(c) Energy decay - standard scale (d) Energy decay - logarithmic scale

Fig. 11. Error metrics for the homogeneous elongated domain excited by an explosive Ricker pulse (f_r = 4 Hz) located at (−10 m, −4 m) (Example 2).

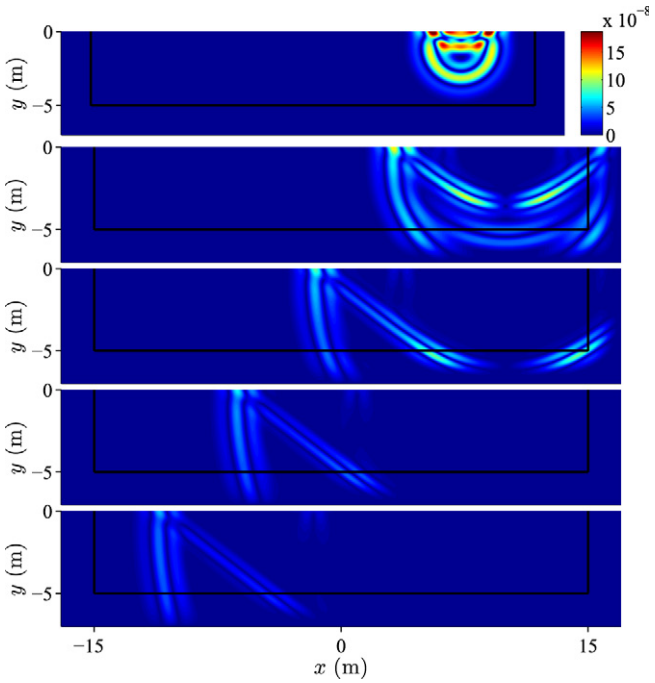

Fig. 12. Snapshots of u taken at t = 0.5, 1.0, 1.5, 2.0, 2.5 s in Example 3 with an explosive near-surface Ricker wavelet source.

attenuation profile. By contrast, lower velocities, higher polynomial orders, or larger R values, tend to broaden the support of the attenuation profile within the PML, thereby reducing the absorption, and, by and large, the accuracy.

To introduce near grazing-angle waves, we modeled a 30 m × 5 m computational domain, surrounded on three of its sides by a 2 m-thick PML, as shown in Fig. 9(a). The explosive source disk was positioned at 4 m below the surface and 5 m to the right of the left PML interface. The PML and regular domain were discretized similarly to Example 1, and resulted in a 20-cell-thick PML. We used $R = 10^{-8}$, a time step of 0.0002 s, and, again, let the simulation run for 10 s.

Snapshots of the displacements (u) are shown in Fig. 10. As discussed above, and contrary to findings reported by others, there is no evidence of spurious energy leaking back into the regular domain: the PMLs have quite efficiently absorbed the waves.[6] Fig. 11(a) displays the comparison of displacement field L^2 norms, while, Fig. 11(b) shows the normalized relative error $e(t)$ in percent. The peak relative error value is about 0.4% and occurs when the P-front reaches the right-side PML interface, causing small reflections (the continuous PML form is reflection-less, but the discrete PML is not). Fig. 11(c) and (d) show that the energy decay is

[6] It has been reported often that spurious energy appears at the tail of the transient phase, and is only observable when the response is capped at a very small fraction (∼0.001) of the peak response amplitude. Modifying the PML parameters has been reported to have an effect on the spurious energy, but parameterization guidelines remain elusive. The CPML and the more recent M-PML both improve the behavior, but the issue is still open.

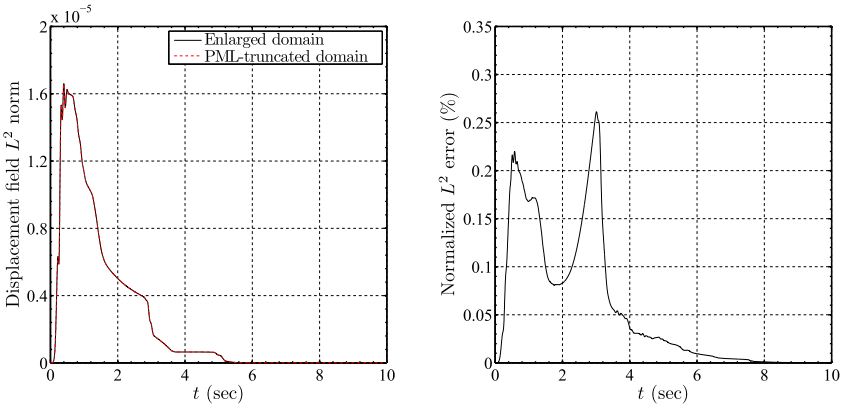

(a) Displacement field norm $D(t;\Omega^{\mathrm{RD}})$ (b) Relative error $e(t)$

Fig. 13. Error metrics for the homogeneous elongated domain excited by an explosive Ricker pulse ($f_r = 4$ Hz) located at (10 m, −1 m) (Example 3).

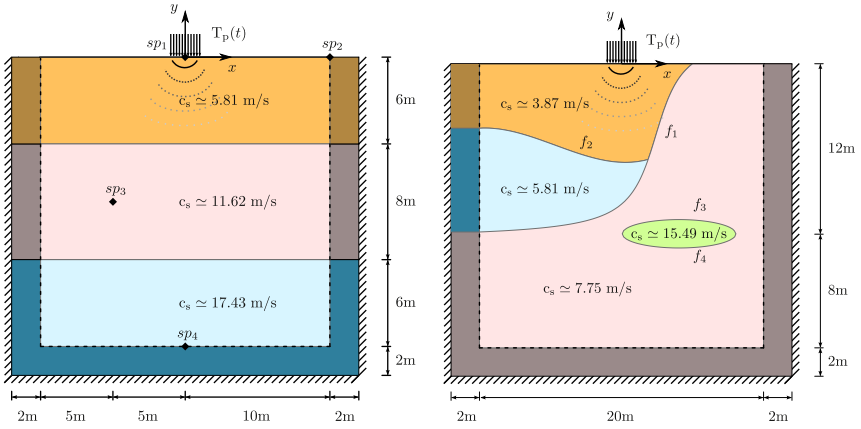

(a) Layered medium (b) Arbitrarily heterogeneous medium

Fig. 14. PML-truncated semi-infinite media in two dimensions subjected to surface loads.

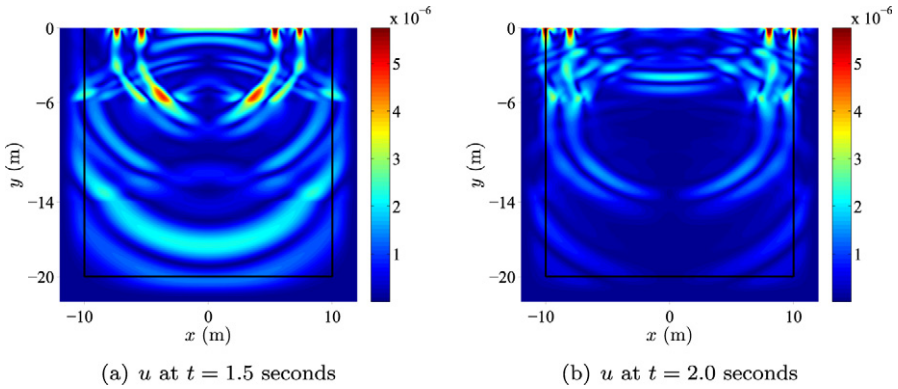

(a) u at $t = 1.5$ seconds (b) u at $t = 2.0$ seconds

Fig. 15. Snapshots of u for the layered domain (Example 4).

more gradual in this case than in Example 1, though the overall behavior is qualitatively similar to the one reported in Example 1. As a consequence of the direction of the propagation, which is mostly parallel to the bottom interface, initially it is only the bottom PML that imposes attenuation. Once the waves reach the right-side PML, the absorption is complete.

Example 3. Prior studies [44,55] have noted the efficacy of the PML in absorbing surface waves. Using the geometry and discretization of Example 2, we relocated the source excitation 1 m below the surface, as shown in Fig. 9(b) in order to corroborate the findings of previous works, and test our own formulation with surface waves. Fig. 12 shows snapshots of the displacement (u). These results are consistent with those of other studies and suggest that our mixed, unsplit-field PML can effectively absorb and attenuate surface waves too. Similar to Example 2, the displacement field L^2 norm and the time-dependent relative error are shown in Fig. 13. Although not presented here, the energy decay is gradual for the same reasons as those previously described.

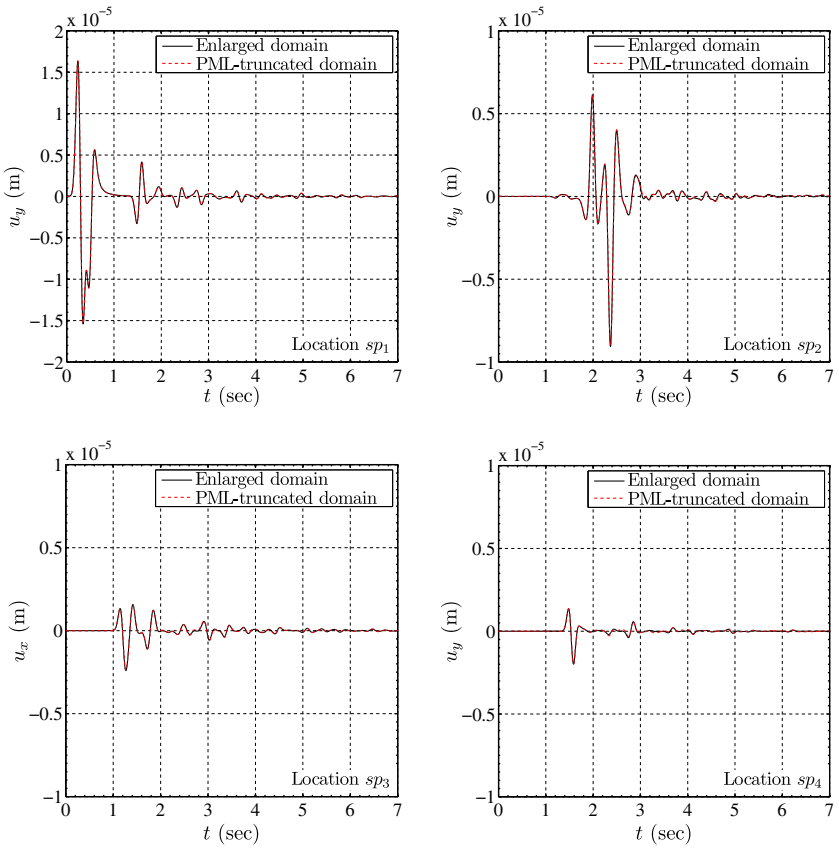

Fig. 16. Comparison of u_x and u_y time histories between the enlarged and PML-truncated domain solutions at various sampling points (Example 4).

5.2. Heterogeneous media

To illustrate the performance of the PML in heterogeneous media, we consider next two simulations: first a layered profile, and then an arbitrarily heterogeneous profile with an inclusion. We apply a surface stress load over a region ($-1\text{ m} \leqslant x \leqslant 1\text{ m}$) in both cases. The time signal is a Ricker pulse with a central frequency of $f_r = 4$ Hz and amplitude of 10 Pa (Fig. 3). Using a time step of 0.0002 s, we let the simulations run for 7 s and 10 s for the last two examples, respectively.

Example 4. As shown in Fig. 14(a), we consider a 20 m × 20 m layered medium surrounded by 2 m-thick PML on its sides and bottom. We define

$$c_s(y) = \begin{cases} \sim 5.81\text{ m/s}, & \text{for } -6\text{ m} \leqslant y \leqslant 0\text{ m}, \\ \sim 11.62\text{ m/s}, & \text{for } -14\text{ m} \leqslant y < -6\text{ m}, \\ \sim 17.43\text{ m/s}, & \text{for } -22\text{ m} \leqslant y < -14\text{ m}. \end{cases} \tag{53}$$

The material interfaces were extended horizontally into the PML, thereby, avoiding sudden material changes at the interface between the PML and the regular domain. The PML and regular domains were discretized by quadratic elements with an element size of 0.1 m, whereas in the vicinity of the surface load, the regular domain was meshed with 0.025 m-elements. The reflection coefficient R was set to 10^{-8}.

Fig. 15 shows the snapshots of displacement taken at two different times. The layer boundaries are clearly visible due to reflections at the material interface. However, the critical interface between the regular domain and PML is free of reflections. Extending the layer boundaries into the PML preserved the transparency of the PML-regular domain interface to the outgoing waves.

To further assess the performance of the mixed PML formulation, we compare the displacement time histories at the sampling points against a reference solution obtained using an enlarged domain (200 m × 100 m). Fig. 16 depicts a visual comparison of the response time histories for u_x and u_y at various sp_i points. As it can be seen, the agreement is quite satisfactory. Fig. 17 is the counterpart of Fig. 7 for the heterogeneous case: the highest relative error in the L^2 norm is about 2.7%; though higher than the one we reported for the homogeneous case, we consider it satisfactory. The pointwise errors depicted in Fig. 17(c) and (d) are even better: under the load, the error does not exceed 0.63%, and at the PML-regular domain interface it is less than about 1.75% at all times. Fig. 18 shows that the energy decay is more gradual in this case due to the layered profile (multiple reflections/transmissions) than in the homogeneous domain cases.

Example 5. As in the previous example, we consider a 20 m × 20 m computational domain surrounded by a 2 m-thick PML on its sides and bottom. The profile functions f_1, f_2, f_3, and f_4 were used to define the various interfaces (Fig. 14(b)); they were defined as

$$f_1(x,y) = 4.7\arctan(0.7x - 1.7) - 5, \tag{54a}$$

$$f_2(x,y) = -0.05(x+10)^2 + 0.005(x+8)^3 - 4.5, \tag{54b}$$

$$f_3(x,y) = \sqrt{1 - \left(\frac{x-4}{4}\right)^2} - 12, \tag{54c}$$

$$f_4(x,y) = -\sqrt{1 - \left(\frac{x-4}{4}\right)^2} - 12. \tag{54d}$$

As in Example 4, the material interfaces were extended horizontally into the PML. The reflection coefficient R was again set to

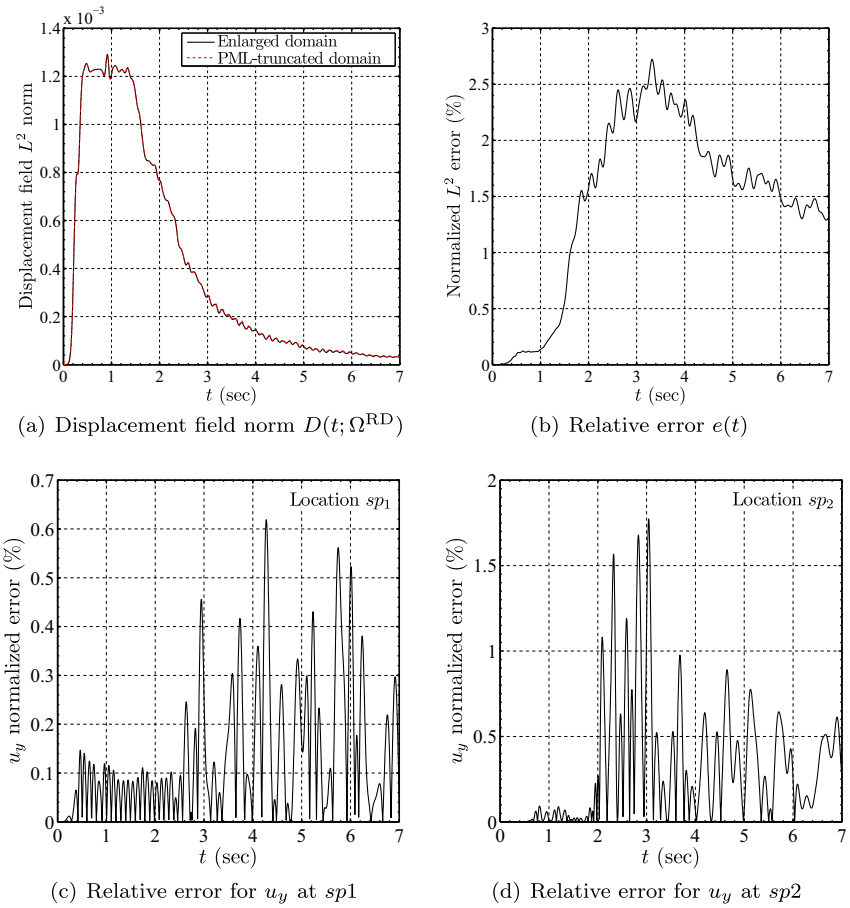

(a) Displacement field norm $D(t;\Omega^{\mathrm{RD}})$ (b) Relative error $e(t)$

(c) Relative error for u_y at $sp1$ (d) Relative error for u_y at $sp2$

Fig. 17. Error metrics for the layered medium excited by a surface Ricker pulse ($f_r = 4$ Hz) (Example 4).

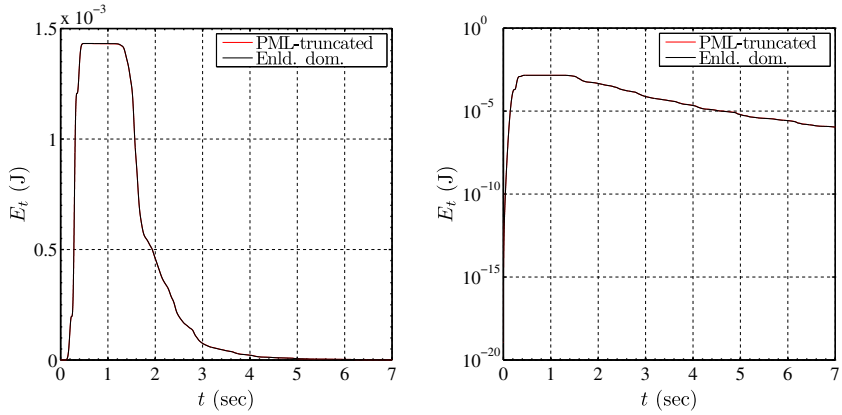

(a) Energy decay - standard scale (b) Energy decay - logarithmic scale

Fig. 18. Total energy decay inside the regular domain (Example 4).

10^{-8}. Fig. 19 shows the snapshots of the displacement taken at two different times. Although there are reflections introduced by the material interfaces, no spurious reflections are observed at the PML interface. Fig. 20 depicts the displacement field L^2 norm and the normalized relative error by comparing the response of the PML-truncated domain against the response obtained using an enlarged domain (150 m × 80 m). The agreement between displacement field norms is again fairly satisfactory. However, the normalized relative error is a few percentage points: until, approximately, $t = 4$ s, the relative error is roughly around 2.6%, which is quite reasonable to expect considering the error metrics obtained for layered media (Example 4). Between about $t = 4$ s and $t = 4.7$ s, the displacement response amplitudes become so small that they interfere with small amplitude reflections from the fixed exterior boundary of the PML. Even the slightest disturbance in the propagation pattern triggers change; after about $t = 4.7$ s, the normalized relative error decreases monotonically as the waves are steadily leaving the computational domain. The energy decay shown in Fig. 20(c) and (d) show good agreement between the reference and PML solutions.

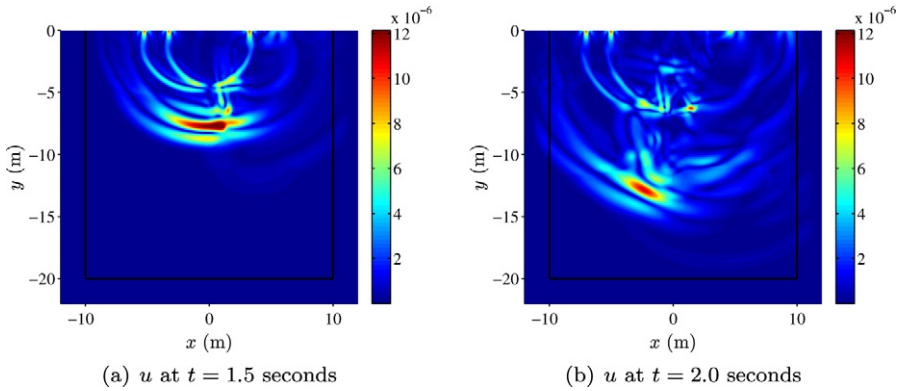

Fig. 19. Snapshots of u for the heterogeneous domain with an inclusion (Example 5).

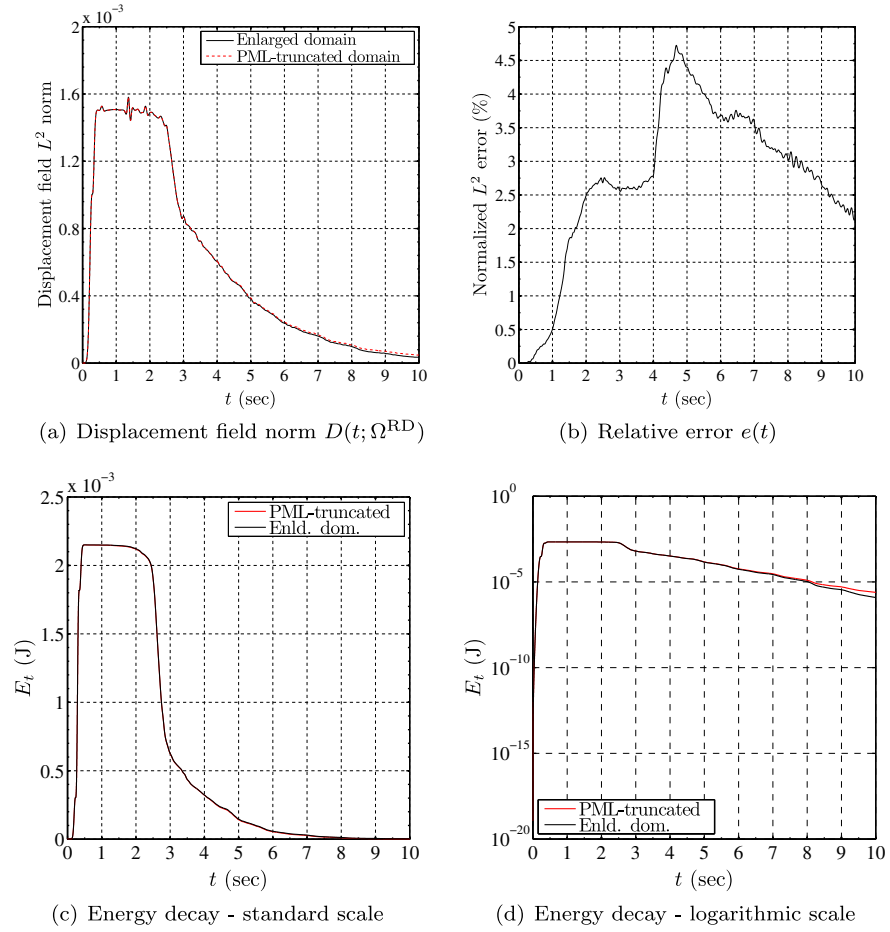

Fig. 20. Error metrics for the arbitrarily heterogeneous medium excited by a surface Ricker pulse ($f_r = 4$ Hz) (Example 5).

6. Conclusions

We discussed a new mixed displacement–stress formulation for the simulation of elastic waves in PML-truncated, arbitrarily heterogeneous media based on a regularly-stretched and unsplit-field PML. Through the introduction of auxiliary variables (stress memories), the resulting semi-discrete forms are second-order in time, thus greatly facilitating time integration.

Despite the increase in the number of unknowns due to the adoption of a mixed method, but owing to the non-splitting of the fields, the associated computational cost is less than that arising in split-field formulations. However, the method remains computationally expensive, due to its mixed nature, when compared to displacement-only formulations, if the latter were at all possible in the presence of a PML. Accommodation of the method in existing displacement-only interior codes requires modifications to account for the mixed form of the interior problem, and, though not difficult, the additional expense makes the method more suitable for new implementations.

We reported numerical simulations demonstrating the stability and efficacy of the approach. The high-quality absorption inside the PML is remarkable and there were no instabilities or other non-causal behavior observed. Both standard isoparametric linear–linear and quadratic-quadratic pairs of approximants proved to be numerically stable, without having to resort to specialized elements (e.g. RT) in order to retain stability.

All simulations were conducted by adhering to the usual rules of thumb for wave simulations, whereby a minimum of 12 points per wavelength are necessary to adequately resolve the wave motion. The minimum expected wavelength was used to drive the mesh density, while simultaneously satisfying the Courant condition. However, we have found and reported that the sharpness of the decay profile within the PML may impose more onerous requirements on the PML's mesh density than those imposed from a wave propagation perspective. Detailed parametric studies are necessary for providing proper guidance on the choice of the PML parameters.

Acknowledgments

Partial support for this work has been provided by the US National Science Foundation under grant awards CMMI-0348484 and CMMI-0619078. The authors are grateful for the support.

References

[1] S.V. Tsynkov, Numerical solution of problems on unbounded domains. A review, Appl. Numer. Math. 27 (4) (1998) 465–532.
[2] D. Givoli, J.B. Keller, A finite element method for large domains, Comput. Methods Appl. Mech. Engrg. 76 (1989) 41–66.
[3] D. Givoli, J.B. Keller, Non-reflecting boundary conditions for elastic waves, Wave Motion 12 (3) (1990) 261–279.
[4] D. Givoli, S. Vigdergauz, Artificial boundary conditions for 2D problems in geophysics, Comput. Methods Appl. Mech. Engrg. 110 (1993) 87–101.
[5] B. Engquist, A. Majda, Absorbing boundary conditions for the numerical simulation of waves, Math. Comput. 31 (139) (1977) 629–651.
[6] A. Bayliss, E. Turkel, Radiation boundary conditions for wave-like equations, Commun. Pure Appl. Math. 33 (1980) 707–725.
[7] R.L. Higdon, Absorbing boundary conditions for elastic waves, Geophysics 56 (2) (1991) 231–241.
[8] D. Givoli, B. Neta, High-order non-reflecting boundary scheme for time-dependent waves, J. Comput. Phys. 186 (1) (2003) 24–26.
[9] L.F. Kallivokas, S. Lee, Local absorbing boundaries of elliptical shape for scalar waves, Comput. Methods Appl. Mech. Engrg. 193 (2004) 4979–5015.
[10] J.-P. Bérenger, A perfectly matched layer for the absorption of electromagnetic waves, J. Comput. Phys. 114 (1994) 185–200.
[11] J.-P. Bérenger, Three-dimensional perfectly matched layer for the absorption of electromagnetic waves, J. Comput. Phys. 127 (1996) 363–379.
[12] W.C. Chew, W.H. Weedon, A 3D perfectly matched medium from modified Maxwell's equations with stretched coordinates, Micro. Opt. Tech. Lett. 7 (1994) 599–604.
[13] S.D. Gedney, An anisotropic perfectly matched layer-absorbing medium for the truncation of FDTD lattices, IEEE Trans. Antennas Propagat. 44 (12) (1996) 1630–1639.
[14] M. Kuzuoglu, R. Mittra, Frequency dependence of the constitutive parameters of causal perfectly matched anisotropic absorbers, IEEE Microwave Guided Wave Lett. 6 (12) (1996) 447–449.
[15] F.L. Teixeira, W.C. Chew, On causality and dynamic stability of perfectly matched layers for FDTD simulations, IEEE Trans. Microwave Theory Tech. 47 (6) (1999) 775–785.
[16] J.A. Roden, S.D. Gedney, An efficient FDTD implementation of the PML with CFS in general media, IEEE Antennas Propagat. Soc. Int. Symp. 3 (2000) 1265–1362.
[17] F.L. Teixeira, W.C. Chew, Complex space approach to perfectly matched layers: a review and some new developments, Int. J. Numer. Model. 13 (2000) 441–455.
[18] L. Knockaert, D. de Zutter, On the stretching of Maxwell's equations in general orthogonal coordinates systems and the perfectly matched layer, Microwave Opt. Technol. Lett. 24 (1) (2000) 31–34.
[19] J. Maloney, M. Kesler, G. Smith, Generalization of PML to cylindrical geometries, in: Proceedings of 13th Annu. Rev. of Prog. Appl. Comp. Electromag., vol. 2, Monterey, CA, 1997, pp. 900–908.
[20] F.L. Teixeira, W.C. Chew, Perfectly matched layer in cylindrical coordinates, Antennas and Propagation Society International Symposium Digest, vol. 3, IEEE, Montreal, Canada, 1997, pp. 1908–1911.
[21] W.C. Chew, J.M. Jin, E. Michielssen, Complex coordinate system as a generalized absorbing boundary condition, in: Proceedings of 13th Annu. Rev. of Prog. Appl. Comp. Electromag., vol. 25, Monterey, CA, 1997, pp. 909–914.
[22] F.L. Teixeira, W.C. Chew, PML–FDTD in cylindrical and spherical grids, IEEE Microwave Guided Wave Lett. 7 (9) (1997) 285–287.
[23] F.L. Teixeira, W.C. Chew, Systematic derivation of anisotropic PML absorbing media in cylindrical and spherical coordinates, IEEE Microwave Guided Wave Lett. 7 (11) (1997) 371–373.
[24] F. Collino, P. Monk, The perfectly matched layer in curvilinear coordinates, SIAM J. Sci. Comput. 19 (6) (1998) 2061–2090.
[25] F. Collino, P.B. Monk, Optimizing the perfectly matched layer, Comput. Methods Appl. Mech. Engrg. 164 (1998) 157–171.
[26] Q.H. Liu, J.Q. He, Quasi-PML for waves in cylindrical coordinates, Microwave Opt. Technol. Lett. 19 (2) (1998) 107–111.
[27] J.-Q. He, Q.H. Liu, A nonuniform cylindrical FDTD algorithm with improved PML and Quasi-PML absorbing boundary conditions, IEEE Trans. Geosci. Remote Sens. 37 (2) (1999) 1066–1072.
[28] L. Zhao, The generalized theory of perfectly matched layers (GT-PML) in curvilinear co-ordinates, Int. J. Numer. Model. 13 (2000) 457–469.
[29] B. Donderici, F.L. Teixeira, Mixed finite-element time-domain method for transient Maxwell equations in doubly dispersive media, IEEE Trans. Microwave Theory Tech. 56 (1) (2008) 113–120.
[30] B. Donderici, F.L. Teixeira, Conformal perfectly matched layer for the mixed finite element time-domain method, IEEE Trans. Antennas Propagat. 56 (4) (2008) 1017–1026.
[31] J.-P. Bérenger, Evanescent waves in PML's: origin of the numerical reflection in wave–structure interaction problems, IEEE Trans. Antennas Propagat. 47 (10) (1999) 1497–1503.
[32] J.A. Roden, S.D. Gedney, Convolutional PML (CPML): an efficient FDTD implementation of the CFS–PML for arbitrary media, Microwave Opt. Technol. Lett. 27 (5) (2000) 334–339.
[33] J.-P. Bérenger, Numerical reflection from FDTD-PMLs: a comparison of the split PML with the unsplit and CFS PMLs, IEEE Trans. Antennas Propagat. 50 (3) (2002) 258–265.
[34] J.-P. Bérenger, Application of the CFS PML to the absorption of evanescent waves in waveguides, IEEE Microwave Wireless Compon. Lett. 12 (6) (2002) 218–220.
[35] E. Bécache, P.G. Petropoulos, S.D. Gedney, On the long-time behavior of unsplit perfectly matched layers, IEEE Trans. Antennas Propagat. 52 (5) (2004) 1335–1342.
[36] D. Correia, J.-M. Jin, On the development of a higher-order PML, IEEE Trans. Antennas Propagat. 53 (12) (2005) 4157–4163.
[37] D. Correia, J.-M. Jin, Performance of regular PML, CFS–PML, and second-order PML for waveguide problems, Microwave Opt. Technol. Lett. 48 (10) (2006) 2121–2126.
[38] Z. Lou, D. Correia, J.-M. Jin, Second-order perfectly matched layers for the time-domain finite-element method, IEEE Trans. Antennas Propagat. 55 (3) (2007) 1000–1004.
[39] W.C. Chew, Q.H. Liu, Perfectly matched layers for elastodynamics: a new absorbing boundary condition, J. Comput. Acoust. 4 (4) (1996) 341–359.
[40] F.D. Hastings, J.B. Schneider, S.L. Broschat, Application of the perfectly matched layer (PML) absorbing boundary condition to elastic wave propagation, J. Acoust. Soc. Am. 100 (5) (1996) 3061–3069.
[41] Q.H. Liu, Perfectly matched layers for elastic waves in cylindrical and spherical coordinates, J. Acoust. Soc. Am. 105 (4) (1999) 2075–2084.
[42] F. Collino, C. Tsogka, Application of the perfectly matched absorbing layer model to the linear elastodynamic problem in anisotropic heterogeneous media, Geophysics 66 (1) (2001) 294–307.
[43] E. Bécache, P. Joly, C. Tsogka, Fictitious domains, mixed finite elements and perfectly matched layers for 2D elastic wave propagation, J. Comput. Acoust. 9 (3) (2001) 1175–1202.
[44] D. Komatitsch, J. Tromp, A perfectly matched layer absorbing boundary condition for the second-order seismic wave equation, Geophys. J. Int. 154 (2003) 146–153.
[45] T. Wang, X. Tang, Finite-difference modeling of elastic wave propagation: a nonsplitting perfectly matched layer approach, Geophysics 68 (5) (2003) 1749–1755.
[46] U. Basu, A.K. Chopra, Perfectly matched layers for time-harmonic elastodynamics of unbounded domains: theory and finite-element implementation, Comput. Methods Appl. Mech. Engrg. 192 (2003) 1337–1375.
[47] U. Basu, A.K. Chopra, Perfectly matched layers for transient elastodynamics of unbounded domains, Int. J. Numer. Methods Engrg. 59 (2004) 1039–1074.
[48] U. Basu, Explicit finite element perfectly matched layer for transient three-dimensional elastic waves, Int. J. Numer. Methods Engrg. 77 (2009) 151–176.
[49] G. Cohen, S. Fauqueux, Mixed spectral finite elements for the linear elasticity system in unbounded domains, SIAM J. Sci. Comput. 26 (3) (2005) 864–884.
[50] G. Festa, J.-P. Vilotte, The Newmark scheme as velocity–stress time-staggering: an efficient PML implementation for spectral element simulations of elastodynamics, Geophys. J. Int. 161 (2005) 789–812.
[51] F.H. Drossaert, A. Giannopoulos, A nonsplit complex frequency-shifted PML based on recursive integration for FDTD modeling of elastic waves, Geophysics 72 (2) (2007) T9–T17.
[52] F.H. Drossaert, A. Giannopoulos, Complex frequency shifted convolution PML for FDTD modelling of elastic waves, Wave Motion 44 (7–8) (2007) 593–604.
[53] E. Bécache, S. Fauqueux, P. Joly, Stability of perfectly matched layers, group velocities and anisotropic waves, J. Comput. Phys. 188 (2003) 399–433.

[54] K.C. Meza-Fajardo, A.S. Papageorgiou, A nonconvolutional, split-field, perfectly matched layer for wave propagation in isotropic and anisotropic elastic media: stability analysis, Bull. Seismol. Soc. Am. 98 (4) (2008) 1811–1836.
[55] G. Festa, S. Nielsen, PML absorbing boundaries, Bull. Seismol. Soc. Am. 93 (2) (2003) 891–903.
[56] D. Komatitsch, R. Martin, An unsplit convolutional perfectly matched layer improved at grazing incidence for the seismic wave equation, Geophysics 72 (5) (2007) SM155–SM167.
[57] I. Harari, U. Albocher, Studies of FE/PML for exterior problems of time-harmonic elastic waves, Comput. Methods Appl. Mech. Engrg. 195 (2006) 3854–3879.
[58] C. Michler, L. Demkowicz, J. Kurtz, D. Pardo, Improving the performance of perfectly matched layers by means of *hp*-adaptivity, Numer. Methods Partial Diff. Eqs. 23 (4) (2007) 832–858.
[59] Roland Martin, Dimitri Komatitsch, Stephen D. Gedney, A variational formulation of a stabilized unsplit convolutional perfectly matched layer for the isotropic or anisotropic seismic wave equation, Comput. Model. Engrg. Sci. 37 (3) (2008) 274–304.
[60] D.N. Arnold, Mixed finite element methods for elliptic problems, Comput. Methods Appl. Mech. Engrg. 82 (1990) 281–300.
[61] F. Brezzi, A survey of mixed finite element method, in: D. Dwoyer, M. Hussaini, R. Voigt (Eds.), Finite Elements Theory and Application, Springer-Verlag, New York, 1988, pp. 34–49.
[62] P.A. Raviart, J.M. Thomas, A mixed finite element method for second order elliptic problems, in: I. Galligani, E. Magenes (Eds.), Mathematical Aspects of the Finite Element Method, Lecture Notes in Mathematics, vol. 606, Springer-Verlag, New York, 1977, pp. 292–315.
[63] C. Johnson, B. Mercier, Some equilibrium finite element methods for two-dimensional elasticity problems, Numer. Math. 30 (1978) 103–116.
[64] F. Brezzi, J. Douglas, L.D. Marini, Two families of mixed finite element methods for second order elliptic problems, Numer. Math. 47 (1985) 217–235.
[65] D.N. Arnold, F. Brezzi, M. Fortin, A stable finite element for the stokes equations, Calcolo 21 (1984) 337–344.
[66] D.N. Arnold, F. Brezzi, J. Douglas, PEERS: a new mixed finite element for plane elasticity, Jpn. J. Appl. Math. 1 (1984) 347–367.
[67] J.T. Oden, J.N. Reddy, On mixed finite element approximations, SIAM J. Numer. Anal. 13 (3) (1976) 393–404.
[68] J.C. Nédélec, Mixed finite elements in R^3, Numer. Math. 35 (1980) 315–341.
[69] D.N. Arnold, J. Douglas, C.P. Gupta, A family of higher order mixed finite element methods for plane elasticity, Numer. Math. 45 (1984) 1–22.
[70] L.D. Marini, An inexpensive method for the evaluation of the solution of the lowest order Raviart-thomas mixed method, SIAM J. Numer. Anal. 22 (3) (1985) 493–496.
[71] J.C. Nédélec, A new family of mixed finite elements in R^3, Numer. Math. 50 (1986) 57–81.
[72] D.N. Arnold, R.S. Falk, A new mixed formulation for elasticity, Numer. Math. 53 (1988) 13–30.
[73] R. Stenberg, A family of mixed finite elements for the elasticity problem, Numer. Math. 53 (1988) 513–538.
[74] L.P. Frasca, T.J.R. Hughes, A.F.D. Loula, I. Miranda, A new family of stable elements for nearly incompressible elasticity based on a mixed Petrov-Galerkin finite element formulation, Numer. Math. 53 (1988) 123–141.
[75] M.E. Morley, A family of mixed finite elements for linear elasticity, Numer. Math. 55 (1989) 633–666.
[76] F. Brezzi, D. Marini, A survey on mixed finite element approximations, IEEE Trans. Magn. 30 (5) (1994) 3547–3551.
[77] E. Bécache, P. Joly, C. Tsogka, An analysis of new mixed finite elements for the approximation of wave propagation problems, SIAM J. Numer. Anal. 37 (4) (2000) 1053–1084.
[78] D.N. Arnold, R. Winther, Mixed finite elements for elasticity, Numer. Math. 92 (2002) 401–419.
[79] E. Bécache, P. Joly, C. Tsogka, A new family of mixed finite elements for the linear elastodynamic problem, SIAM J. Numer. Anal. 39 (6) (2002) 2109–2132.
[80] D.N. Arnold, R. Winther, Mixed finite elements for elasticity in the stress–displacement formulation, in: Z. Chen, R. Glowinski, K. Li (Eds.), Current Trends in Scientific Computing, Contemporary Mathematics, vol. 329, American Mathematical Society, 2003, pp. 33–42.
[81] D.N. Arnold, G. Awanou, Rectangular mixed finite elements for elasticity, Math. Model. Methods Appl. Sci. 15 (9) (2005) 1417–1429.
[82] Z. Chen, Finite Element Methods and Their Applications, first ed., Springer, New York, 2005.
[83] D.N. Arnold, R.S. Falk, R. Winther, Mixed finite element methods for linear elasticity with weakly imposed symmetry, Math. Comput. 76 (260) (2007) 1699–1723.
[84] L.F. Kallivokas, J. Bielak, R.C. MacCamy, A simple impedance-infinite element for the finite element solution of the three-dimensional wave equation in unbounded domains, Comput. Methods Appl. Mech. Engrg. 147 (1997) 235–262.